Powder bed selective laser process (sintering/melting) applied to tailored calcium phosphate-based powders

P. Navarrete-Segado,[a,b] C. Frances,[b] M. Tourbin,[b] C. Tenailleau[c], B. Duployer[c], D. Grossin[a,*]

[a] CIRIMAT, Université de Toulouse, CNRS, 4 Allée Émile Monso, 31432 Toulouse Cedex 4, France

[b] Laboratoire de Génie Chimique, Université de Toulouse, CNRS, 4 Allée Émile Monso, 31432 Toulouse Cedex 4, France

[c] CIRIMAT, Université de Toulouse, CNRS, 118, Route de Narbonne, 31062 Toulouse cedex 9, France.

Abstract. This paper focuses on the tailoring of calcium phosphate powders for their use as powder bed selective laser process feedstock. Hydroxyapatite and chlorapatite were used as starting powders for the preparation of different blends through the addition of graphite as a laser absorptance additive. A methodical study was conducted to compare the processing windows of the blends containing different amounts of graphite through the laser patterning of circular samples. It was found that the addition of graphite increases the process window of the powder blends being the powder without additive non processable. Hydroxyapatite showed a clear phase transition (decreased when using higher volumetric energy density) into other calcium phosphate phases while chlorapatite was demonstrated to be thermally stable during the whole process (examined through X-ray diffraction and vibrational spectroscopies). In parallel, the study evaluating the powder blend composed of hydroxyapatite and graphite for the production of solid and complex parts was carried out although it required long printing times. The productivity of the process was improved by modification of printing parameters. Then, a series of solid samples were produced for the analysis of the microstructure and mechanical properties. High interconnected porosity was observed in the samples which could improve the bioactivity of the bioceramic scaffolds. A post-treatment of the parts increased their proportion in the hydroxyapatite phase and their mechanical properties. These results are expected to contribute to the application of powder bed selective laser processing of calcium phosphates powders toward bone tissue engineering.

*Corresponding author: david.grossin@ensiacet.fr

Abbreviation list

A = Absorptance

AM = Additive manufacturing

AMCSD = American mineralogist crystal structure database

APS = Atmospheric plasma spray

CIF = Crystallographic information framework

ClA = Chlorapatite

COD = Crystallography open database

CT = X-ray computed tomography

ESEM = Environmental scanning electron microscope

FEG = Field emission gun

FTIR = Fourier-transform infrared

G = Graphite

HA = Hydroxyapatite

HA_Cyl = Calcium phosphate cylinders

HA_Cyl_PT = Calcium phosphate cylinders after post-treatment.

ICSD = Inorganic crystal structure database

LFD = Large field detector

OA = Oxyapatite

PBF = Powder bed fusion

PBSLP = Powder bed selective laser process

PGT = Princeton gamma-tech

PSD = Particle size distribution

R = Reflectivity

Ra = Roughness average

SEM = Scanning electron microscopy

T = Transmission

TA6V = Titanium alloy with aluminium and vanadium

TTCP = Tetracalcium phosphate

UV-Vis = Ultraviolet

XRD = X-ray diffraction

α-TCP = α-Tricalcium phosphate

Symbols

R_b = Bragg error [%]

R_{exp} = Residual exponential distribution [%]

R_{wp} = Weighted residual profile [%]

E_d = Volumetric energy density [J.cm^{-3}]

h = Hatching distance [cm]

k = Thermal conductivity [M.m^{-1}.K^{-1}]

Sig = Sigma [%]

x_{10} = The 10th percentile [μm] (diameter of a sphere at which 10% of the particles in the sample are smaller)

x_{50} = Median particle size [μm] = the 50th percentile (diameter of a sphere at which 50% of the particles in the sample are smaller)

x_{90} = The 90th percentile [μm] (diameter of a sphere at which 90% of the particles in the sample are smaller)

P = Laser power [W]

t = Layer thickness [cm]

v = Scanning speed [cm.s^{-1}]

1. Introduction

The inclusion of ceramics as material feedstock in powder bed fusion (PBF) (ISO/ASTM 52900) additive manufacturing (AM) technologies made the traditional terms to define the process selective laser sintering and selective laser melting inaccurate. The mechanism occurring during the densification of ceramics processed by a laser source is not completely examined. Some materials can experience change in their compositions before sinter/melt (sintering understood as solid state diffusion and not partial melting), and moreover both phenomena can occur as result of increasing the temperature [1]. Recently, the term powder bed selective laser process (PBSLP) has been proposed to avoid a misusing of the previous terms to define the technique [1].

The production of calcium phosphate scaffolds through PBSLP has been largely studied [1]. The printed bioactive scaffolds would serve as the starting point for the growth of new bone for bone replacement applications. Three main strategies have been followed by researchers for the shaping of bioceramic powders through PBSLP.

The first strategy consisting of the use of polymeric powders (e.g., polyethylene, poly-ϵ-caprolactone, and poly (L-lactic acid)) filled with calcium phosphate powders has been widely studied [2–5]. The polymer as the main component in the powder feedstock is melted through the laser irradiation giving as result the printed polymer/ceramic composite scaffold. Since these polymers are not removed after the PBSLP process, the time of implantation can have some adverse effects, thus losing some of their properties or affecting negatively to the tissue regeneration [6].

A second strategy is based on the use of a more similar ratio of polymer /ceramic components to print green body (polymer/ceramic composite) scaffolds. These are then submitted to pyrolysis (of the sacrificial polymer) and sintering steps to obtain the final sintered bioceramic scaffold free of the polymer [7].

The third strategy is the use of the bioceramic powder directly as the main component in the PBSLP process feedstock [8]. In this case, the material interacting with the laser is the ceramic powder whose response will be highly influenced by the type of laser-equipped in the PBSLP apparatus. The laser beam energy has to be absorbed and transformed into heat to trigger the sintering/melting of the powder. Different materials show different absorptance levels depending on the wavelength of the laser used. It is known that ceramic insulators (e.g. calcium phosphates) mainly absorb the light energy emitted by CO_2 lasers ($\lambda = 10600$ nm) however it is not the case when using a fiber laser source ($\lambda = 1070$ nm). The second one is the most common laser-equipped in PBSLP apparatus since it is greatly absorbed by metals, which are the most explored material feedstock in PBSLP technology. For this reason and because of the high cost of the PBSLP equipment there is a significant demand for the development of ceramics adapted to this kind of

laser increasing the number of suitable materials feedstock for the same printer. The addition of absorptance additives has been studied as a method to deal with the observed low absorptance by oxide ceramic materials of fiber laser energy needed for their processing. Carbon graphite-based filler has been demonstrated to increase the fiber laser absorptance by adding small amounts in the material feedstock making possible the printing of oxide ceramics [9,10].

The energy input of the process is defined as volumetric energy density (E_d) (J.cm^{-3}) and different formulations have been considered for its calculation [1]. Most of the current research on process optimization considers the equation (1) for its calculation, which will be used in the present study. However, caution should be given when using E_d since recent works already showed that this equation gives only an approximate estimation and further analyses on the hatch parameters and material properties should be done for a correct evaluation of the energy density [11].

$$E_d = \frac{P_{laser}}{v_{scan} \cdot h_{space} \cdot t_{layer}} \qquad (1)$$

Where P_{laser} is the laser power (W), v_{scan} the scanning speed (cm.s^{-1}), h_{space} is the hatching distance (cm), and t_{layer} is the layer thickness (cm). Recently, Leo et al. [12] remarked the importance of the laser defocus (positive and negative sense) for the process since it has a significant effect on the final microstructure by varying the spot size and for hence the E_d. In particular, when working at low laser power (~38 W), they found that small variations in the defocus value induced significant changes in the part properties. It is then of vital importance the study of the different PBSLP parameters for each material feedstock to find a processing window showing better sintering/melting phenomena of the powder, thus obtaining high-quality parts.

The goal of the present work was to evaluate the performance of different graphite-filled powder blends feedstock with calcium phosphates, such as hydroxyapatite (HA) and chlorapatite (ClA), as main component in a PBSLP process. The use of ClA in addition to HA was explored due to its known higher thermal stability which could be an interesting advantage for processes involving high temperatures [13,14]. Indeed, the ClA conversion into HA has been demonstrated to be feasible through hydrothermal ion exchange of Cl$^-$ by OH$^-$ if the application requires it [15].

Then, the study started with the preparation of calcium phosphate powders feedstock through the addition of different amounts of graphite as an absorptance additive. The processability of the different powder feedstock was tested in a PBSLP process at different printing conditions to observe the influence

of the E_d in the final sample properties (e.g. phase transition, surface finishing…). The comparison between the different powders and parameters was possible through the examination of the chemical and structural composition, morphology, and mechanical properties of the printed samples. Additionally, a thermal post-treatment was carried out on the solid samples to study its effect on their composition and macro-structural properties.

2. Materials and method

2.1 Materials

Hydroxyapatite (HA) microspheres powder was used as the main component for the production of the powder blends that will be used as material feedstock for the PBSLP process. This initial powder was produced by Urodelia (SA Company, Saint-Lys, France) via wet-chemical coprecipitation and a posterior spray-drying process (product reference 300.08.2). More information about the wet-chemical approach followed was offered in a previous work [16]. Moreover, the spray drying process of hydroxyapatite powders was covered previously with a deeper examination of the HA microspheres flowability in a previous work [17]. The spray drying step was crucial to produce the flowable HA powder composed of spherical agglomerates.

In addition, pure chlorapatite (ClA) powder was produced through a solid-gas reaction (chlorination) of the initial HA powder in a tubular furnace. The procedure followed was already described in the work of Demnati et al. [18]. This ClA powder was also used as the main component for the preparation of blends employed as PBSLP process feedstock.

Different powder blends were produced by mixing graphite as an absorptance additive with HA and ClA powders as main components. TIMREX® KS 44 Graphite by Imerys is a carbon graphite-based filler that acts as a near-infrared absorptance additive improving the laser-material interaction of the powders. The preparation of the blends was carried out by pouring the previously weighted amounts of powders (a total of 0.5 kg) in a mixing jar, then the powders were mechanically blended using a Turbula shaker mixer at 42 rpm for 1 hour. A list of the acronyms referring to the raw and prepared powder blends is given in Table 1.

Table 1. Acronyms for different raw materials and blends feedstock used during our study.

Powder/blend acronym	Description
HA	Hydroxyapatite microspheres used as raw material.
ClA	Chlorapatite microspheres used as raw material.
G	Graphite flakes used as raw material (absorptance additive).
HA_5G	Powder blend composed of hydroxyapatite and a 5 wt. % of graphite.
HA_10G	Powder blend composed of hydroxyapatite and a 10 wt. % of graphite.
ClA_5G	Powder blend composed of chlorapatite and a 5 wt. % of graphite.

TA6V discs with one side coated by plasma spray with HA (0.1 mm coating thickness) were used as a substrate to improve the attachment of the first printing layers to the building platform surface. The dimensions of the discs were 10 cm in diameter, 2 mm of TA6V thickness. They were produced by the company 2PS (Projection Plasma Système, Montbazens, France), which is specialized in plasma projection coating of orthopedic implants.

2.2 Characterization methods

2.2.1 Chemical and structural analyses

Different characterization techniques were used to confirm the chemical and structural composition of the raw and produced materials. X-ray diffraction (XRD) analyses of both powders and printed samples were performed in a BRUKER's X-ray diffractometer D8 Advance system with Cu Kα radiation (wavelength $\lambda = 0.15406$ nm), a nickel filter at 40 kV and 40 mA, and a LYNXEYE XE-T detector (energy resolution of 0.38 keV). Samples were analysed using a 6 mm x 2 mm slit in a 2θ range between 20º and 90º, a step of 0.03º 2θ, and a time per step of 0.2 s.

Rietveld refinement method was applied to estimate the crystalline phase compositions of the different printed samples containing a multiphase calcium phosphate mixture of hydroxyapatite (HA) $Ca_{10}(PO_4)_6(OH)_2$, alpha-tricalcium phosphate (α-TCP) $(Ca_3(PO_4)_2$, tetracalcium phosphate (TTCP) $Ca_4(PO_4)_2O$, and graphite (C) phases. MAUD (Material Analysis Using Diffraction) software (written by Luca Lutterotti [19]) was used for the diffraction analyses. The following methodology was followed to estimate the phase compositions of the multiphase samples. Rietveld refinements were performed in a 2θ range between 21º and 36º. This range was chosen to include the main reflections of each phase. All samples were refined assuming the possible presence of the four phases, and the crystallographic information

frameworks (CIF) of the standard single-phase standards were employed for the refinement (phase/database/code: HA/AMCSD/0002281; Graphite/AMCSD/0000049; α-TCP/COD/2106194 TTCP/ICSD/2631). Seven background points were settled for the calculation of the complete background curve via linear interpolation.

Fourier transform infrared spectroscopy (FTIR) analyses were performed to determine the chemical composition of powders using a spectrometer FTIR iS50 and the KBr pellet preparation method. About 9 mg of powdered sample was transferred to a clean mortar, then a weighed amount of dry KBr powder (300±5 mg) was added and homogenously mixed. A compression at 6000 kg was employed to produce the sample disk used for the analysis. FTIR spectra were recorded in the 4000-400 cm^{-1} wavenumber range using a step width of 0,48 cm^{-1}.

A Horiba-Jobin Yvon Labram HR 800 Raman spectrometer provided with 633 nm laser excitation was used to obtain the Raman spectra of the samples during our study. For reference, standard Raman spectra have been obtained from the RRUFF™ Project database for pure HA (RRUFF id: R100225, 780 nm), and ClA (RRUFF id: R060192, 780 nm). Raman spectra from TTCP and α-TCP were obtained through the analyses of reference samples produced in the laboratory.

2.2.2 Morphological and structural properties

The particle size distribution (PSD) of the different powders used in this work was analysed in dry conditions with a Mastersizer MS 3000 (Malvern Panalytical®) laser particle size analyser. For the analyses, the powder was dispersed at a venturi pressure of 0.1 bar. Refractive indexes for the different powders were taken as 1.63 (HA), 1.65 (ClA), 2.70 (graphite) while the absorption indexes were 0.01 (HA), 0.01 (ClA), 1 (graphite). The morphology of powders was investigated with a scanning electron microscope (SEM) LEO 435 VP (Leica®) equipped with a Ge detector (Imix-PC, PGT) after metallization of the ceramic surface with a thin film of silver using a Scancoat Six sputter coater. Printed samples were analysed in a FEI ESEM Quanta™ 450 FEG, an environmental scanning electron microscope (ESEM) used with a large field detector (LFD) in low vacuum (LowVac) mode without previous metallization of the surface of the sample. ImageJ was used for the processing of the images [20].

High-resolution X-ray micro-computed tomography (CT) analyses of the HA cylinders were performed in a phoenix nanotom® equipped with a 180 kV / 15 W high-power nanofocus X-ray tube (9 µm voxel size, resolution). A 3D perspective of the cylinders was reconstructed and it was possible to examine their

total porosity. VGStudio MAX 4.4 software was used to reconstruct the data sets and visualize the objects three-dimensionally.

The geometrical density of the cylinders was calculated from the mass and dimensions of at least ten samples. For comparison, the density of the parts was also measured by Archimedes' method in distilled water as liquid.

2.2.3 Laser absorptance of powders

Diffuse reflectance spectra were collected using a double beam spectrophotometer AGILENT® Cary 5000 UV/Visible/NIR and integration sphere accessory of 110 mm. Before the measurements, predetermined photometry calibration was made using specimens with known reflectance. Experimental data were collected within the 900-1200 nm range with 1 nm step and 0.5 s integration time. Powders were compacted in the sample holder and were approximatively 3 mm thick. The absolute transmittance and reflectance can be measured directly with high accuracy and the absorptance can be obtained from these by a simple calculation:

$$A = 1 - R - T \qquad (2)$$

Where A represents absorptance, R is reflectance and T is transmittance (which is considered equal to zero). A predetermined photometry calibration was made using specimens with known reflectance. Three different samples (N=3) were taken for each blend and were measured obtaining the mean value and the standard deviations (mean ± standard deviation) evaluating their homogeneity.

2.2.4 Mechanical properties of HA cylinders

The procedure followed for the analysis of the compression strength of the HA cylinders is described in ISO 13175-3:2012 [21]. The compression strength of the printed cylinders before and after thermal post-treatment was measured in an MTS Criterion® Model 42 electromechanical universal test system. An MTS load cell model LSB.203, with a capacity of 2000 N was used to measure the shear force at a crosshead speed of 0.085 mm/s at room temperature. Samples were submitted to a pre-stress of -3N to avoid any irregularity due to the state of the sample surface before starting the compression test. The measurements were stopped manually once the cylinder collapsed. The samples were set in the middle of the plate vertically inverted to the printing orientation. Since it was a preliminary study, a low number of measurement repetitions were performed: three post-treated cylindric samples (N=3, mean ± standard deviation) and one as-printed.

2.3 PBSLP process

PBSLP process of the blend powders was performed in a 3D Systems ProX® DMP 200. Parts are built up layer by layer sintering/melting the powder particles by a laser which is directed to the powder particles. The laser follows the pre-loaded 3D model building selectively the subsequent horizontal layers. The manufacturing process is then carried out by joining each new layer to the previous one.

The main components present in the manufacturing chamber of the printer are illustrated in Figure 1. A roller (with 110 mm of diameter) which can move in a straight line using a carriage (speed of 400 mm/s, accuracy <1 mm) and rotate (with speed 3.7 turns per second, accuracy <5°) carry out the actions of layering such as spreading, smoothing, and compacting. The layer thickness of powder can differ depending on the material properties (particle size, flowability…). A scraper enables to carry the powder from the feeding piston to the sintering piston. The feeding piston contains the powder reservoir used for sintering (140 x 140 mm, powder volume: 3.85 liters). Parts are manufactured on the TA6V discs coated with HA (which are glued onto the sintering plate which is positioned on plate support on the sintering piston (140 x 140 mm). A collecting tank recovers all non-sintered powders and residues that can be treated for recycling. Since no material is removed, waste is reduced significantly. It is a Class I Laser System. The main optical devices are a fiber laser source (continuous operation, single-mode, power at the collimator output 300W, wavelength in the shortwave infrared range (approx. 1070 nm), a collimator (outlet beam diameter at $1/e^2$ 15 mm), a scanner head, and a flat field F-Theta lens (420 mm focus length). This configuration gives a beam diameter of the focal spot of 38.1 µm. A preliminary trial-and-error study of the powders' processability allowed us to enclose the parameters range used in the present study. These are described in Table 2.
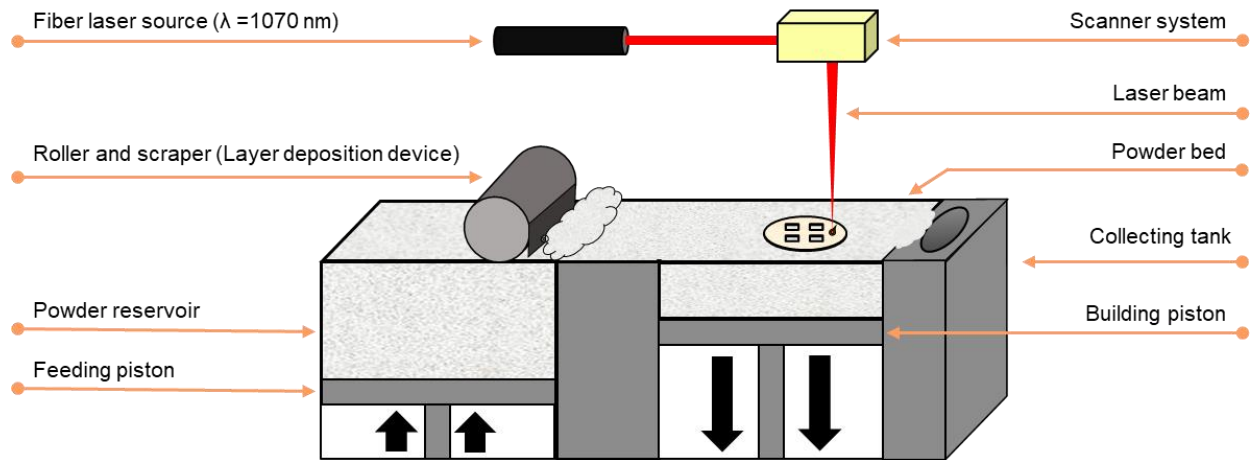

Figure 1. Schematic illustration showing main components present in the manufacturing chamber of a 3D Systems ProX® DMP 200 printer.

Table 2. Fixed and studied parameters for the determination of the processing window of the PBSLP
process in the present work.

	Parameter	Value
Studied	Fiber laser power (W)	30-54
	Scan speed (mm/s)	25-125
	Laser scan strategy	Hexagonal & Zig-Zag (5 laser passes) (90° rotation between layers)
Fixed	Hatching distance (mm)	0.05
	Layer thickness (mm)	0.10
	Atmosphere	Air
	Powder compression (%)	300
	Laser defocus	3 cm downward of the focus plane
	Printing substrate	HA-coated TA6V disc
	Chamber preheating	No

Three different approaches were performed in parallel to study the influence of the printing parameters and feedstock formulation. For each of the approaches different 3D models were used for the printing of the samples, also they were printed with two different laser scanning strategies. These two laser scanning strategies are illustrated in Figure 2.
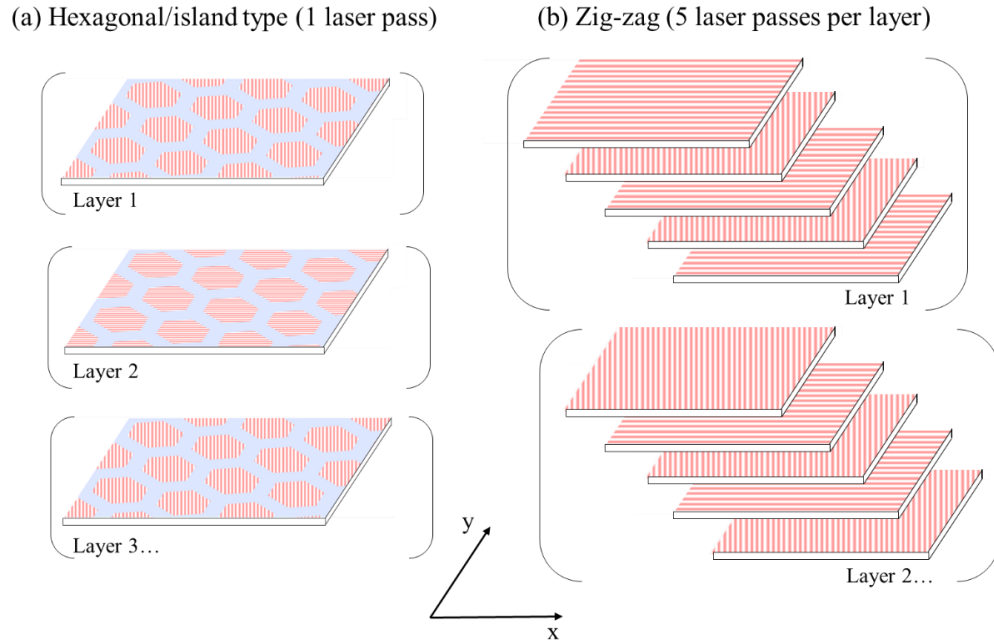
Figure 2. Schematic diagram of the two laser scanning strategies used during the three approaches: (a) Hexagonal/island type scanning (1 laser pass per layer) and (b) zig-zag scanning (5 laser passes per layer). In red the pattern followed by the laser scans and the blue regions refer to the overlap between hexagons.

The three kinds of samples together with the strategies followed for each approach are described below:

- The first approach, laser-induced circular patterns: The 3D model consisted of a short cylinder of 8 mm of diameter and 0.8 mm of height. In this case, the laser scan strategy used was a hexagonal (island type) strategy (Figure 2a). The continuous hexagons had 0.2 mm of diameter and overlap between them of 0.1 mm. The orientation of the hexagons was rotated 90º between layers. This kind of sample was conceived to study the influence of the printing parameters (or E_d) and evaluate the process window of the different powder blends. This specific sample design allowed us to shorter the printing times and to perform different characterization techniques (XRD, Raman, SEM…) directly on the substrate. Once the samples were produced, compressed air was used to clean the surface of the disk to remove the raw material particles settled on the samples.

- The second approach, HA complex shape: In parallel to the previous approach, the printing of two different 3D models with increased shape complexity was evaluated. One model consisted of a cylindrical scaffold (20 x 17 mm) with controlled internal porosity while the second one was based on a trapezoid with a toothed bottom surface (8 x 25 x 13 mm). The same hexagon-

based laser scan strategy as in the first approach was used (Figure 2a). However, only one combination of laser parameters was tested (laser power: 30 W, scanning speed: 25 mm/s, E_d: 240 J.cm^{-3}) for both parts. The model used for these samples was designed to test the printing feasibility of 3D complex parts with a set of printing parameters. After printing, a homemade endless diamond wire saw was used to detach the scaffold from the substrate while for the trapezoid it was not necessary thanks to its toothed bottom surface.

- The third approach, HA cylinders: A cylinder of 10 mm of diameter and 15 mm of height was used as a 3D model (taking into account the dimensions needed for mechanical tests which are described in ISO 13175-3:2012). The E_d and laser parameters combination used for the printing was obtained from the results of the first approach studying the process window (laser power: 36 W, scanning speed: 75 mm/s, E_d: 96 J.cm^{-3}). Due to the low building rate of the hexagonal-based laser strategy for the printing of solid parts (second approach), a new laser scan strategy of zig-zag was used to increase it (Figure 2b) (the building rates obtained for the second and third approaches will be discussed in the next section). Because the overlapping of laser passes in the same region seemed to enhance the final result, an overlapping of 5 laser passes per layer over the same irradiated region was used. The orientation of the laser tracks was rotated between both passes and layer steps. The model used for these samples was designed to perform a posterior compression strength test as well as chemical and structural characterization. After printing, it was possible to detach the HA cylinders from the substrate by hand without modifying their surface.

A list of the acronyms referring to the printed samples corresponding to each of the three different approaches followed is given in Table 3.

Table 3. Acronyms for different printed samples in each of the three approaches followed during our study

Approach	Printed sample acronym	Description
First approach	HA_5G_96	Laser-induced circular pattern produced at 96 J.cm^{-3} with a powder blend composed of hydroxyapatite and a 5 wt. % of graphite.
	HA_10G_57.6 / 96 / 288	Laser-induced circular patterns were produced at 57.6, 96, and 288 J.cm^{-3} with a powder blend composed of hydroxyapatite and a 10 wt. % of graphite.
	ClA_5G_96 / 336	Laser-induced circular pattern produced at 96, and 336 J.cm^{-3} with a powder blend composed of chlorapatite and a 5 wt. % of graphite.
Second approach	HA_Scaffold	Calcium phosphate scaffold complex part produced at 240 J.cm^{-3} with a powder blend composed of hydroxyapatite and a 5 wt. % of graphite.
	HA_Trapezoid	Calcium phosphate trapezoid complex part produced at 240 J.cm^{-3} with a powder blend composed of hydroxyapatite and a 5 wt. % of graphite.
Third approach	HA_Cyl	Calcium phosphate cylinders produced at 96 J.cm^{-3} with a powder blend composed of hydroxyapatite and a 10 wt. % of graphite.
	HA_Cyl_PT	Sample HA_Cyl after thermal post-treatment.

2.4 Thermal post-treatment

A posterior thermal post-treatment was performed at air presence for the HA cylinders to study the changes in their chemical and structural properties as well as in their mechanical properties. The cylinders were placed between two alumina crucibles which were set in the middle of the muffle Nabertherm® LT 9/13 furnace chamber favouring a more homogeneous heat distribution. The temperature programme consisted of a heating ramp of 2ºC/min till a temperature of 1250ºC. This temperature was kept constant for 2 hours before starting the cooling phase (-1ºC/min).

3. Results and discussion

3.1 Characterization of raw/prepared powders and substrate

The PSD and the SEM micrographs of each of the three raw powders (HA, ClA, and graphite) used for the preparation of the PBSLP feedstock materials are illustrated in Figure 3. It can be observed how the ClA and the HA powders have almost similar properties. It demonstrates that the chlorination of the HA powder to obtain ClA powder does not modify their morphology keeping unaltered the PSD and the spherical shape of the agglomerates. The graphite powder is composed of flakes with smaller median particle size and a more dispersed distribution.
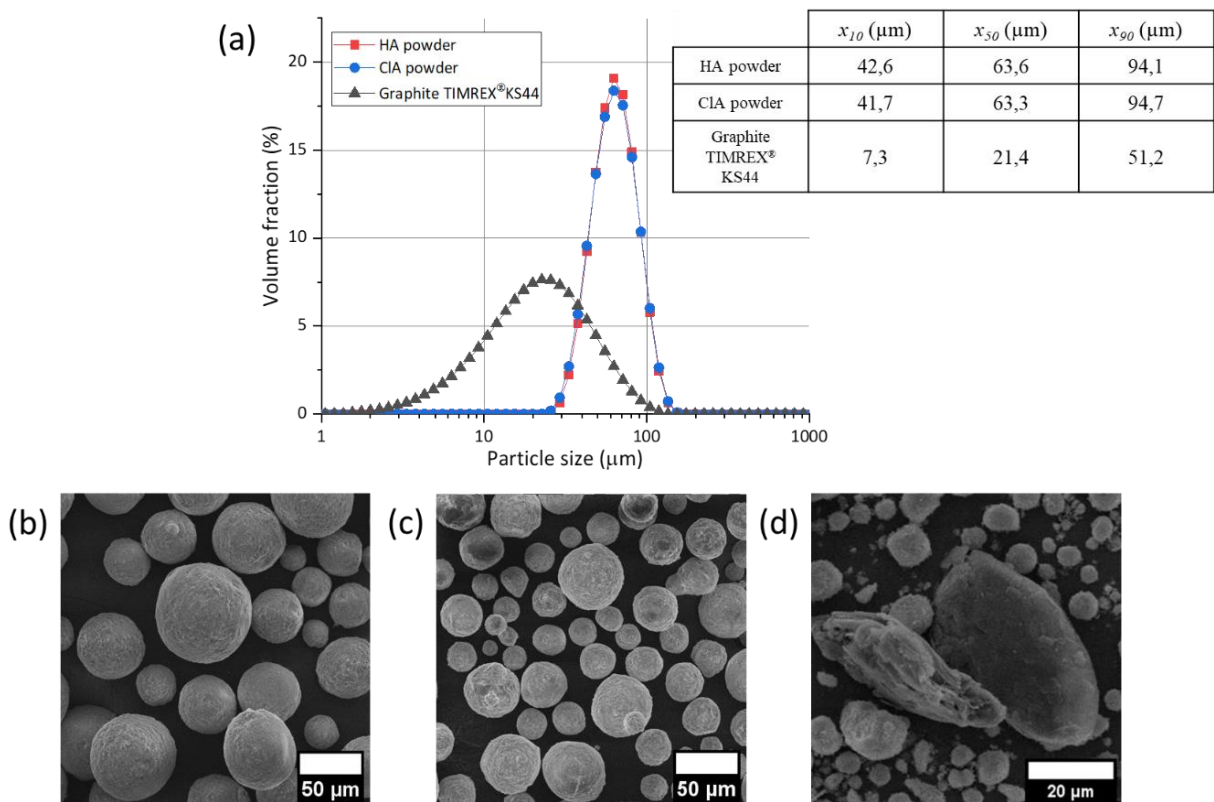
Figure 3. (a) Particle size distributions and SEM micrographs of (a) HA, (b) ClA microspheres, and (d) graphite flakes (in a blend) used as raw materials

.

The obtained Raman spectra and X-ray diffractograms of the initial ceramic powders are offered in Figure 4 and Figure 5, respectively. For reference, standard Raman spectra have been obtained for HA (RRUFF id: R100225), and ClA (RRUFF id: R060192) from the RRUFF™ Project database. The chemical and structural composition of each of the initial powders was confirmed. We can point out the presence of both monoclinic and hexagonal phases in the ClA diffractogram. This partial phase change could be

produced during its synthesis since it is known that ClA undergoes a phase change from hexagonal to monoclinic upon heating at 200-300 ℃ [14].
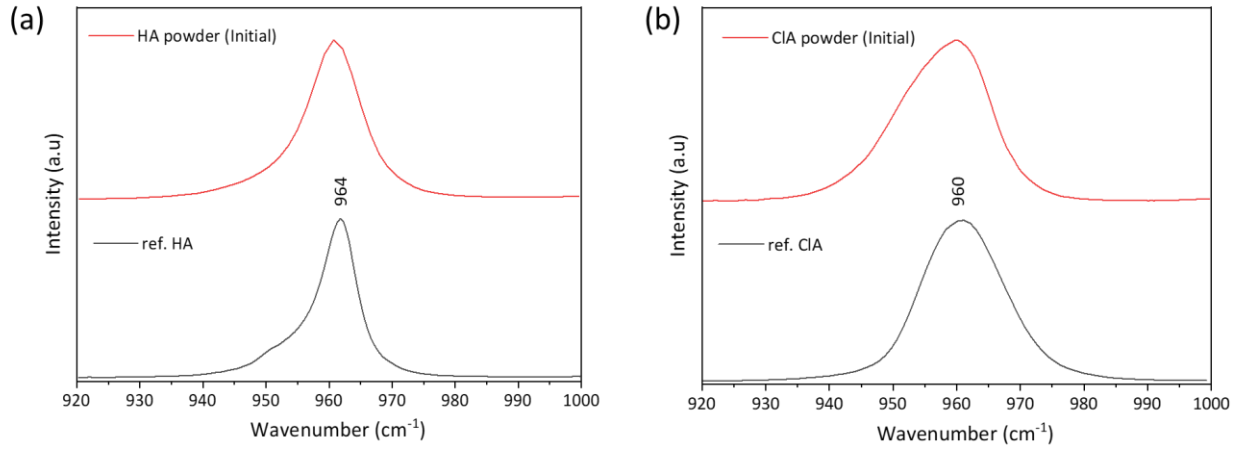

Figure 4. Raman spectra were obtained for the initial ceramic powders used in our study. For reference Raman spectra for (a) HA (RRUFF id: R100225), and (b) ClA (RRUFF id: R060192) were obtained from the RRUFF™ Project database.
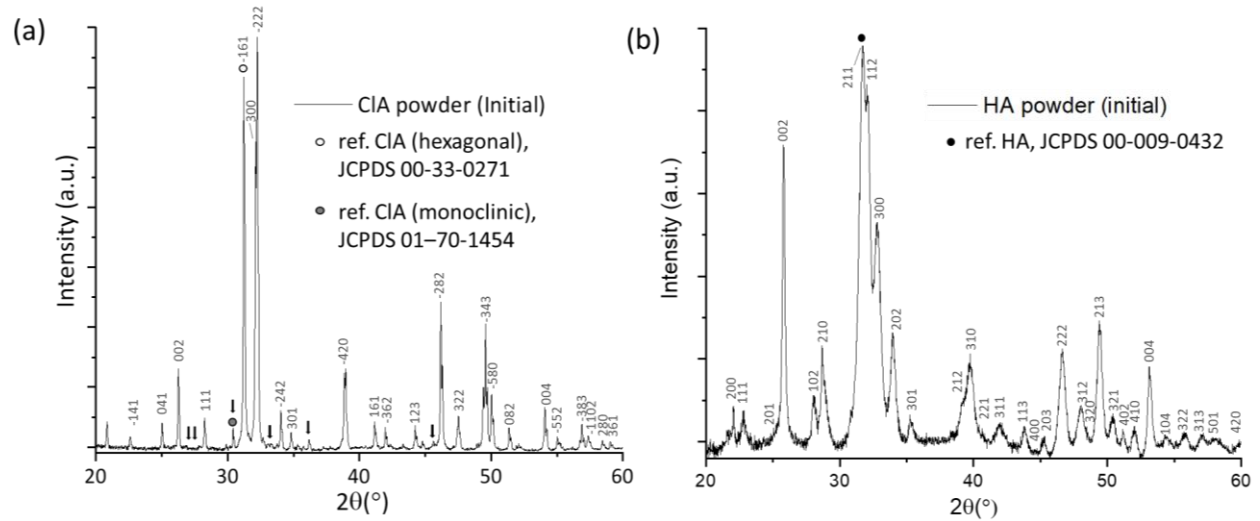

Figure 5. XRD diffractograms obtained for the initial (a) ClA and (b) HA ceramic powders used in our study. Reference patterns: ClA (hexagonal) JCPDS 00-33-0271, ClA (monoclinic) JCPDS 01-70-1454, and HA JCPDS 00-009-0432. Superlattice lines on ClA pattern are shown by arrows.

The study of the powdered material absorptance at a certain laser wavelength is of particular interest for the PBSLP process because it allows one to determine the processing window suitable for sintering or melting. Tolochko et al. [22] carried out an exhaustive study on the laser absorption of different materials stating that the absorption mechanism has a complex character and it depends on the kind of material (metals, ceramics…). Even for the same material, it can vary from one spectral region to another. They explained that the laser sintering of a single-component powder is a complicated process since the sintering processing window can be very narrow. The particles either do not sinter staying as loose powder or undergo a complete melting at high power density that leads to the formation of resolidified droplets due to the liquid surface melt contraction. They also studied the addition of water-soluble powders such as $NaNO_3$ and $NaCl$ to metal/ceramic powders as absorption additives. After laser sintering of the blend, the sintered parts could be immersed in water to dissolve the added substance, controlling the porosity of the part by adding different additive volume fractions. They concluded that the greater the absorptance of a powder, the less the laser energy density needed for the sintering. For this reason, absorption additives have gained special relevance in PBSLP, while they should be carefully selected for the improvement of the product properties.

For the present study, powdered graphite was chosen as the second component in our blends. Its application as an absorption additive has also been evaluated previously showing promising results [9,23,24]. It highly absorbs the laser beam energy emitted at the fiber laser near-infrared wavelength ($\lambda = 1.070$ µm) equipped in our printer and can transform it into heat to sinter/melt the powder feedstock. The mechanism expected for its burnout and removal will be detailed below.

The absorptance of the different pure and powder blends used in this work was determined before their use. The absorptance values obtained are shown in Table 4. Different clear changes in powder colour were observed since HA was initially white but after its chlorination, it produced a yellowish ClA powder increasing its laser absorptance from 2.37% to 12.51%. Then, after the addition of graphite to produce the blends, powders became greyish (darker with the increase of graphite proportion). Results showed an increase of the powder absorptance from 2.37% of pure HA to 66.83% and 73.73% when containing 5% and 10% wt. of graphite, respectively, demonstrating its capacity as absorption additive.

Table 4. Determined absorptance at the emitted wavelength (1070 nm) of the fiber laser light for the powders used as PBSLP feedstock. (N=3, mean ± standard deviation)

Material	Absorptance at λ = 1070 nm (%)
HA	2.4±0.1
HA_5G	66.8±0.1
HA_10G	73.7±1.1
ClA	12.5±0.1
ClA_5G	69.2±0.0
G	80.5±0.1

Figure 4 shows the SEM micrographs of the HA coating surface on TA6V discs used as a substrate during the printing process. The HA coating homogeneity is observed for the whole disc surface and surface roughness can be also appreciated at higher magnification, which is common for the atmospheric plasma spray (APS) process [25,26]. For example, high roughness average (Ra) values in between 4.4 and 5.4 µm have been observed for the same kind of HA coatings produced by APS in previous works [27].
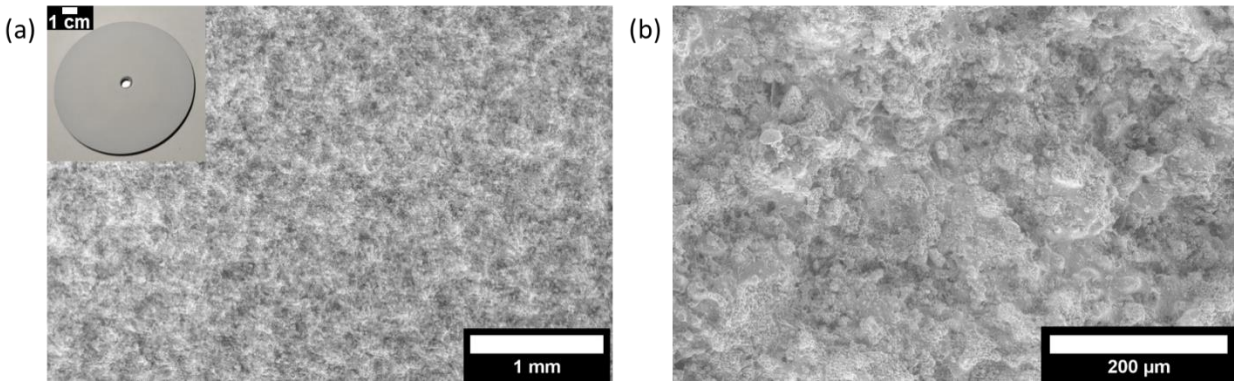

Figure 6. SEM micrographs of HA coating surface on TA6V discs used as a printing substrate.

3.2 Analyses and evaluation of PBSLP samples

3.2.1 First approach: Laser-induced circular patterns.

The printing of circular patterns was used as a faster method to evaluate the performance of the printing parameters as well as the influence of the powder feedstock formulation. The printed single circular patterns obtained with different powder feedstock and E_d can be observed in Figure 7. The corresponding PBSLP process windows are shown in Figure 8. The surrounding circles indicate the samples that will be characterized more in detail for comparison of powder feedstock and E_d (HA_5G_96 / HA_10G_57.6 / HA_10G_96 / HA_10G_288 / ClA_5G_96 / ClA_5G_336). Three quality criteria were used to identify and evaluate macroscopically the different parameters performance at each assigning point: no densification, sintered/melted powder, and thermal cracking. When the laser energy is not enough it does not produce densification of the powder, in absence of sintering/melting phenomena it results in loose particles. Instead, too much energy can induce different adverse effects on the powder bed such as thermal cracks (due to high thermal gradients and stresses) with the impossibility of forming solid parts.
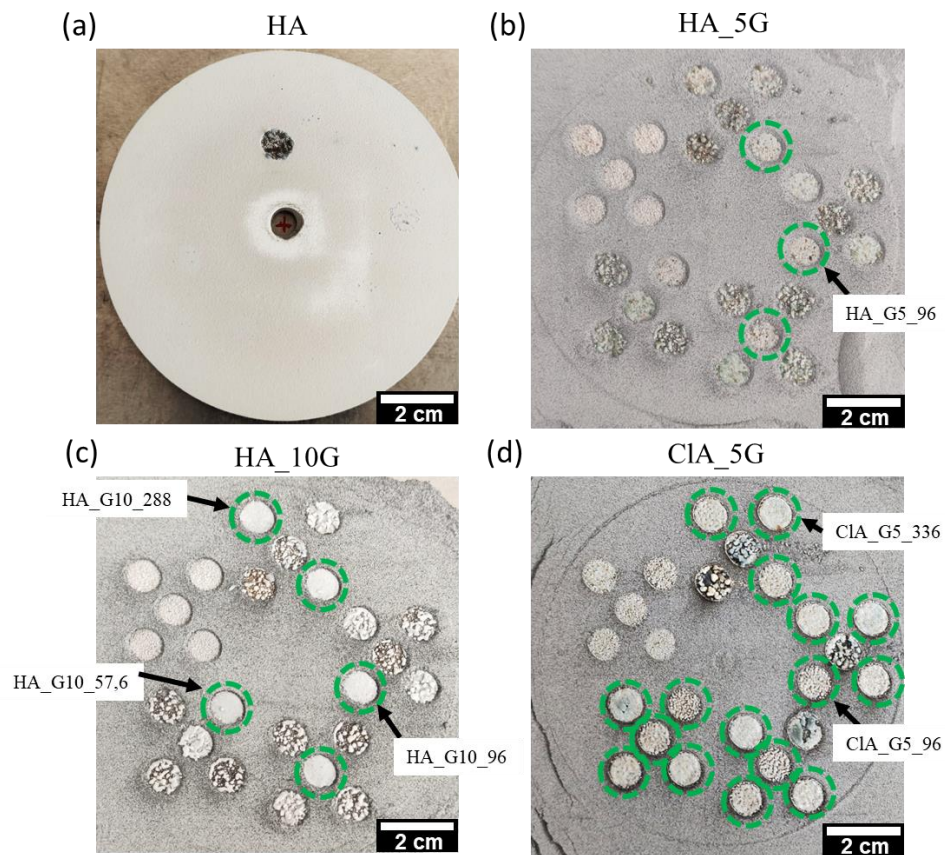

Figure 7. The single circular patterns were obtained for different powder feedstock and printing parameters: (a) HA, (b) HA_G5, (c) HA_10G, (d) ClA_5G. (Process window study)

In the case of pure HA powder, no densification was observed for the whole range of parameters studied. The majority of the set of parameters did not show any kind of interaction between the powder and the laser. Only at the highest laser power and lowest scanning speed (432 J.cm^{-3}), the powder bed was spattered and the HA coating was removed from the substrate.

Between the process windows obtained for HA_5G and HA_10G, we could observe that the range of parameters in which a correct powder sintering/melting occurred was relatively narrow. However, for the powder containing a higher amount of graphite the process window seemed to be enlarged, thus indicating that a higher number of laser parameters (E_d range) can properly sinter/melt the powder. As we mentioned above, the higher the amount of graphite in the blend the better the interaction of the laser with the powder blend thus leading to a better surface finishing.

It is also important to point out that for the same HA_10G powder blend, we could observe some cases in which samples treated at constant energy density the result depends on the laser speed and laser power used. It is the case for the samples produced with 36 W, 75 mm.s^{-1} and 48 W, 100 mm.s^{-1}. Both produced the same energy density (96 J.mm^{-3}) however only the first sample showed a proper sintering/melting of the powder. Even if the energy density remains constant, it is known that the combination of laser hatch distance, laser scanning speed, and laser power has a significant influence [11]. These three tuneable laser parameters do not have the same effect in the printed parts. Laser scanning has the lowest effect, followed by the hatching distance, and the laser power having the highest influence [28]. These different degrees of influence are not considered in the concept of laser energy density. For this reason, the energy density should not be the only criterion in the optimisation of the process parameters and additional parameters should be indicated (e.g. laser scanning strategy, laser defocus…) [11].

The enlargement of the process window is even more notorious when changing the calcium phosphate powder to ClA. It is known that ClA is more stable than HA. This higher thermal stability is given by the anion substitution in the hexagonal axis of the apatite structure [14]. ClA melts at 1530ºC while HA powders are reported to be sintered up to a theoretical density at 1000–1200 °C. The drawback is that the processing (sintering/melting) of HA is difficult due to the presence of the OH content, which decomposes to form TCP and anhydrous calcium phosphates at ~1200–1450 °C leading to grain growth. Indeed, the water present in the sintering atmosphere can inhibit HA densification and accelerates grain growth. The decomposed phases will trigger different dissolution rates, when present in physiological conditions [29]. For this reason, ClA has been studied as a substitute for HA in other manufacturing processes involving high temperatures (e.g. plasma spraying) [13].
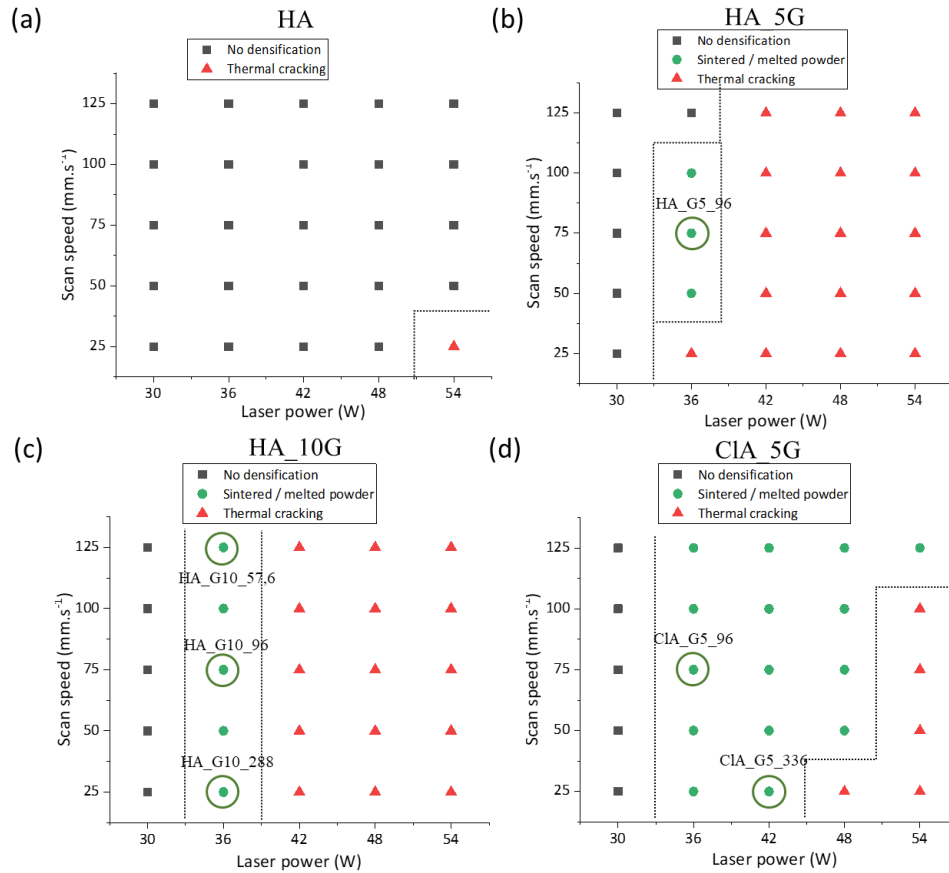
Figure 8. PBSLP process window comparison of the different powder feedstock: (a) HA, (b) HA_5G, (c) HA_10G, and (d) ClA_5G. The surrounding circles indicate the posteriorly characterized samples for comparison.

The SEM analyses of the circular pattern microstructures produced at the same E_d (96 J.cm^2) and using different powder feedstock blends are shown in Figure 9. The three different laser-induced circular pattern samples showed a balling effect. It is a common unfavourable defect in laser processing of both ceramics and metallic materials which has been widely studied [30,31]. Gu et al. [32] defined two different types of balling phenomena:

- The first type of balling phenomenon is defined by coarsened balls giving an interrupted dendritic structure having an inherent structural weakness. It gives as results a rough surface and is caused by a limited liquid formation and low undercooling degree of the melt because of a low laser input. A schematic representation of the process forming this first type of balling phenomenon is illustrated in *figure eight* in the reference Gu et al. [32].

- The second type is defined by numerous micrometric balls over the region irradiated by the laser. These balls should not be confused with the HA or ClA microspheres used as raw material which

had a smaller size. In addition, the smoother surface of the balls is an indication that these are produced as a product of a melting process. Its initiation is attributed to the melt splashes due to a high capillary instability of the melt [33]. A schematic representation of the process forming this first type of balling phenomenon is illustrated in *figure nine* in the reference Gu et al. [32].

For the sample defined as HA_10G_96, the second type of balling phenomenon can be identified due to the presence of numerous micrometric balls on the surface. In this case, the surface irradiated remained flat apart from the presence of the balls. The ClA_5G_96 sample showed instead signals of the first type of balling effect having a higher surface roughness but the number of micrometric balls was lower. Finally, the sample HA_5G_96 showed a combination of both kinds of phenomena. The differences in laser absorptance and powder stabilities could produce different melting behaviours resulting in different surface finishing.

At higher magnification, pinholes (about 20 µm diameter) can be observed randomly distributed over the whole surface of the samples. We could hypothesize that the formation of these pinholes could be due to the formation of micro gas bubbles of CO and CO_2 as a product of the graphite burnout which diffuses leaving a space. The reasons supporting this idea are that the size of the graphite flakes ($x_{50} = 21.4$ µm) fits well with the size of the observed pinholes and their number is increased when higher amounts of graphite are present in the blend. However, further efforts should be made on the study of the effect of increasing the quantity of graphite on the porosity of the samples.
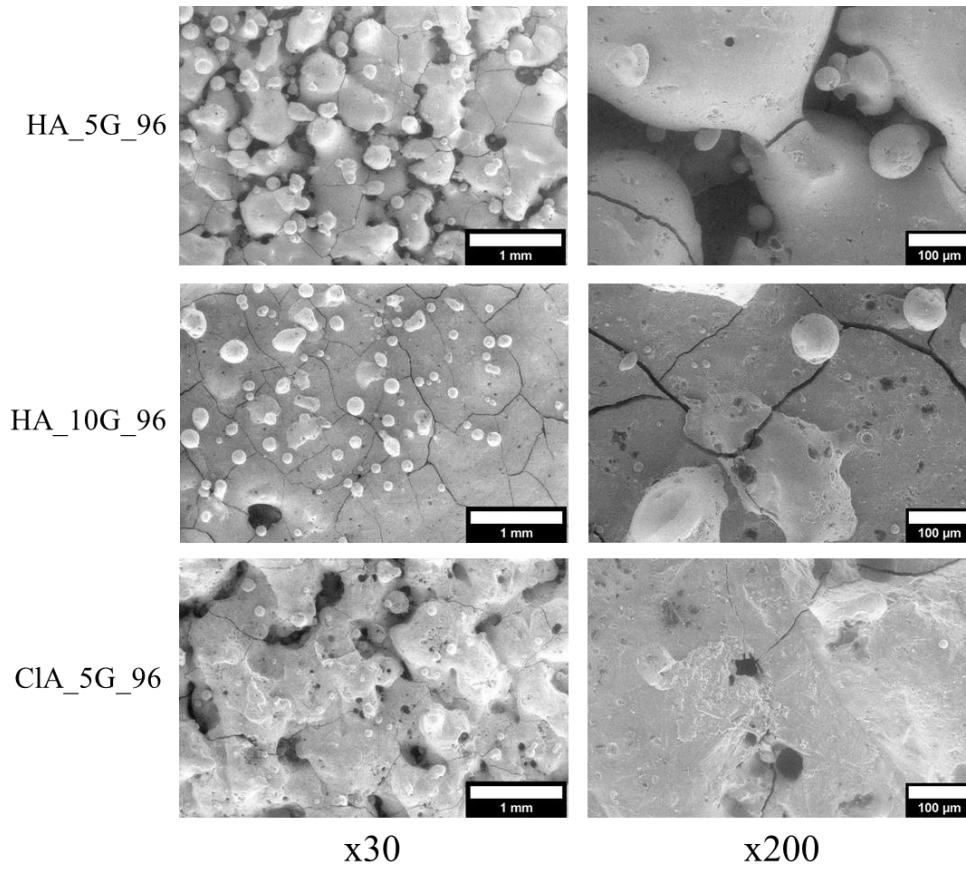
Figure 9. SEM analyses of laser-induced circular patterns produced at same Ed (96 J.cm^{-3}) with different powder feedstock blends: HA_5G_96, HA_10G_96, ClA_5G_96.

The comparison of the microstructures of the samples produced using HA_10G feedstock blend at different E_d is offered in Figure 10. The samples produced at higher E_d (288 J.cm^{-3} and 96 J.cm^{-3}) showed both the second type of balling phenomenon (apparition of molten micrometric balls). However, in the sample printed at lower E_d (57.6 J.cm^{-3}), the surface showed a clear diminution of the number of balls produced, indicating a diminution of the splashing of molten balls. The surface finishing of this last one was found to be flatter due to the absence of balls. The grain boundary cracking (2D defects) in the surfaces of the three kinds of samples was detected. Grain boundaries are known to have a strong effect on the propagation of cracks and the generation of impurity-controlled porosity. At high temperatures, they are also the main starting point for the deformation in polycrystalline ceramics [34]. An increase in the dimensions of the grains and cracking incidence was observed when increasing the E_d used during the process.
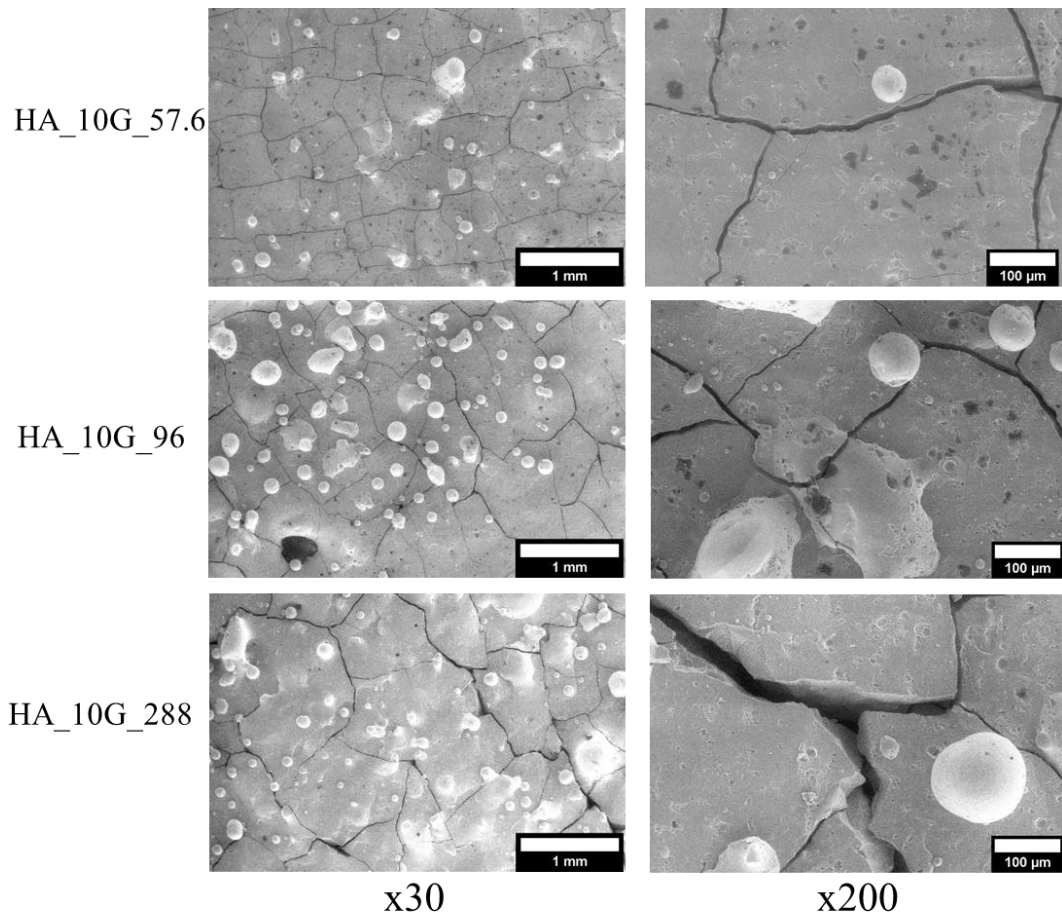
HA_10G_57.6

HA_10G_96

HA_10G_288

x30 x200

Figure 10. SEM analyses of laser-induced circular patterns produced with same powder feedstock blend (HA_10G) at different E_d: 288 J.cm^{-3}, 96 J.cm^{-3}, 57.6 J.cm^{-3}. Analyses of sample HA_10G_96 are repeated here for better comparison.

The ClA sample produced at higher E_d (ClA_5G_336) was analysed for comparison. Figure 11 shows the resulting microstructure. This increase in E_d diminished the presence of the first type of balling phenomenon giving the sample a flatter surface compared with the ClA sample at lower E_d (Figure 9). Holes with approximatively 100 µm of diameter are distributed randomly over the surface. Most of these holes are filled with stick-shaped ClA particles parallel to the surface plane. This ClA particle morphology has been previously observed after the treatment of ClA at high temperatures [35,36].
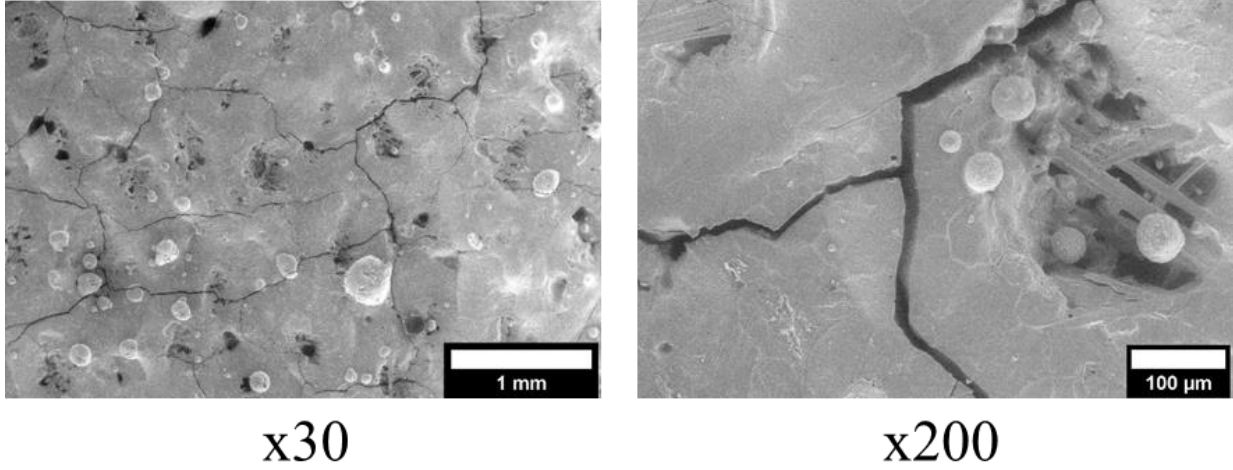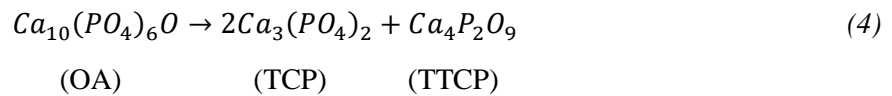
ClA_5G_336

x30   x200

Figure 11. SEM analyses of laser-induced circular patterns produced with ClA_5G feedstock blend at
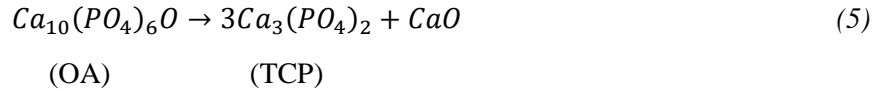*$E_d = 336$ J.cm^{-3}.*

The chemical and structural composition of the previous samples was analysed for comparison by Raman and XRD analyses. Figure 12a shows the comparison between the Raman spectra of the circular patterns obtained from different feedstock powders at the same printing parameters. For samples in which HA was used as main component feedstock (HA_5G and HA_10G), it was found that the most significant contributions come from the strongest spectral bands corresponding to the $v_1 PO_4$ vibration of TTCP (961, 956, 946, 940 cm^{-1}), α-TCP (976, 964, 954 cm^{-1}), and HA (964 cm^{-1}) can be observed. This indicates that a phase transition occurred during the PBSLP process due to the high temperature reached. HA dehydroxylation into oxyapatite (OA) occurs at about 900ºC in air [14]:

$$Ca_{10}(PO_4)_6(OH)_2 \rightarrow Ca_{10}(PO_4)_6O + H_2O \tag{3}$$

(HA)   (OA)
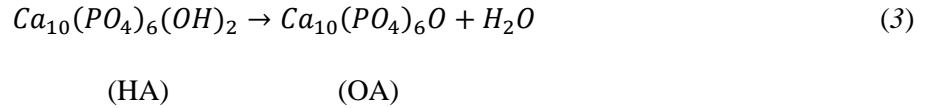
Then, two outcomes are stoichiometrically possible above 1050 ºC: (i) a mixture of TTCP and TCP (β-TCP at temperatures below 1200ºC or α-TCP at higher temperatures) or (ii) a mixture of TCP and CaO by the following reactions [14]:

$$Ca_{10}(PO_4)_6O \rightarrow 2Ca_3(PO_4)_2 + Ca_4P_2O_9 \tag{4}$$

(OA)   (TCP)   (TTCP)

and

$$Ca_{10}(PO_4)_6O \rightarrow 3Ca_3(PO_4)_2 + CaO \qquad\qquad (5)$$

$$\text{(OA)} \qquad\qquad \text{(TCP)}$$

We could hypothesize that the temperature reached during the process is higher than 1200ºC. A slight difference can be observed between the relative intensities of the bands for the spectra of these two samples, thus indicating a different proportion between phases present in the samples. For the sample prepared from the feedstock ClA_5G, only the band corresponding to the v_1PO_4 vibration of ClA (960 cm^{-1}) was observed, indicating that there was no visible alteration of the phase.

Figure 12b shows the comparison between the Raman spectra obtained from samples produced with the same powder feedstock (HA_5G) but at different printing parameters. The Raman bands of the three studied spectra corresponded again with the v_1PO_4 vibration of TTCP (961, 956, 946, 940 cm^{-1}), α-TCP (976, 964, 954 cm^{-1}), and HA (964 cm^{-1}). In this case, no clear variation between the relative intensities of the bands was observed. Therefore, the calcium phosphate phases obtained in the three samples resulted in having very similar proportions for the range of parameters studied.

It should be pointed out that small variations on intensity and shift of bands can be due to several reasons such as:

- If the band is characteristic of more than one compound, then the intensity would be the contribution of these compounds.
- The crystal orientation can affect the relative intensity of the characteristic Raman band of a compound.
- HA and ClA reference spectra were obtained at different laser radiation (780 nm) to the rest of the samples (622 nm).
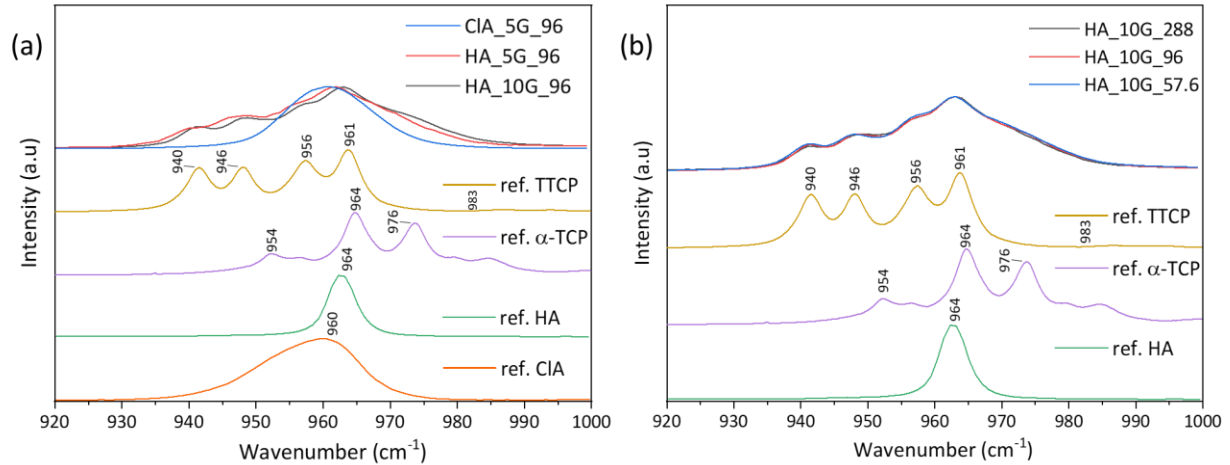
Figure 12. Raman spectra were obtained for the laser-induced circular samples printed with (a) different powder feedstock and (b) different printing parameters.

Figure 13a shows the X-ray diffractograms of the circular samples produced with powder blends of HA and different amounts of graphite (HA_5G_96 and HA_10G_96) at the same energy density $(E_d = 96$ J.cm$^{-3})$. The diffractogram of the initial HA powder was added for comparison. Both samples showed a phase transition. A combination of HA, TTCP, α-TCP, and graphite phases was observed in both diffractograms. However, differences in the relative intensities of the peaks were detected. This indicates that the proportion between phases is different depending on the sample. It is important to note the possibility of having more phases present in the samples, for example, subproducts from the decomposition of the present phases, however, they could be in quantities too low to be detected.

Figure 13b shows X-ray diffractograms of the initial HA powder and the samples printed with the powder blend of HA and 10 wt. % of graphite (HA_10G_57.6, HA_10G_96, and HA_10G_288) with different energy densities. The comparison between the peaks corresponding to graphite indicates that its diminution is higher with the increase in energy density. It could be caused by a more significant burnout of the graphite particles due to the higher temperatures generated. Regarding the calcium phosphate phases present in the samples, the three of them showed a HA transition into TTCP and α-TCP. Another difference between the diffractograms was the unlike HA crystals orientation depending on the energy density used. A lower energy density seemed to induce a higher preference on the HA crystals orientation to the (002) plane (peak at 25.70º). However, since it is found out of the scope of this study no further investigations were done on the laser-induced texture of HA crystals.

Figure 13c shows the XRD diffractograms of the sample printed with the powder blend of ClA and 5 wt. % (ClA_5G_96) at 96 J.cm^{-3} and the initial ClA powder. The analysis did not show a phase transition

from ClA into other calcium phosphate phases, however, a phase transition from monoclinic to hexagonal ClA was detected. A preferred crystals orientation or crystallographic texture to the 002 plane is also clearly visible for this sample. In addition, a small amount of graphite was observed in the sample apart from ClA.
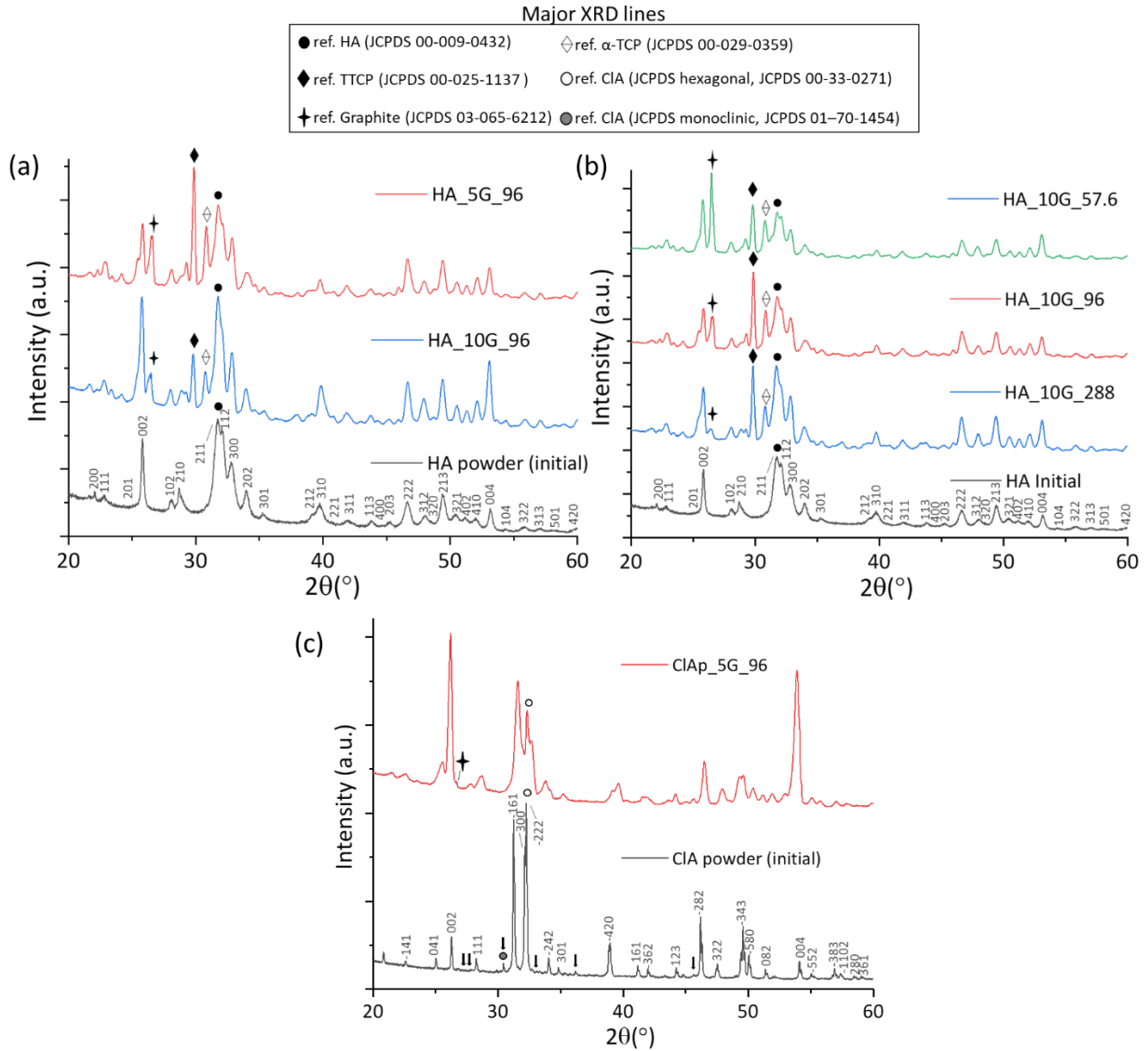

Figure 13. X-ray diffractograms were obtained for the laser-induced circular samples printed with (a) HA with different amounts of graphite (5 and 10 wt. %), (b) at different printing parameters, and (c) using chlorapatite with 5 wt. % graphite as feedstock. Superlattice lines on ClA pattern are shown by arrows.

The Rietveld refinement method was performed to quantify the different phases present in the HA samples after the phase transition. Plots of the Rietveld refinement of the samples analysed are offered in Figure S1. Table 5 shows the refined phase compositions and reliability factors obtained through Rietveld refinement for the calcium phosphate printed samples.

Table 5. The refined phase compositions and reliability factors for the calcium phosphate printed samples.

	Mean Rietveld composition (wt. %)			
Sample	HA_5G_96	HA_10G_57.6	HA_10G_96	HA_10G_288
HA (wt. %)	48.1±0.3	28.0±1.6	35.5±0.9	46.5±2.0
TTCP (wt. %)	13.2±0.1	13.7±0.6	25.5±0.6	19.90±0.9
α-TCP (wt. %)	33.2±0.5	50.1±2.1	31.1±0.8	29.0±1.3
Graphite (wt. %)	5.5±0.1	8.1±0.2	7.8±0.0	4.6±0.3
Sig (%)	2.19	8.03	3.63	3.74
R_b (%)	1.15	3.29	1.64	1.65
R_{wp} (%)	1.68	5.12	2.49	2.74
R_{exp} (%)	0.77	0.64	0.68	0.72

The sample containing less amount of graphite (HA_5G_96) was the one showing the highest HA amount (48.1%) to the other phases, thus indicating that the sample experimented a weaker phase transition during the PBSLP process. For the samples containing the same level of graphite but printed at different scanning speeds *(HA_10G_57.6 / HA_10G_96 / HA_10G_288),* some differences were observed in the calcium phosphates proportions. The remaining amount of HA has a clear tendency to increase when the scanning speed is lower (higher energy density) indicating that a lower phase transition occurred at lower scanning speeds during the process (46.5 wt.% HA at 25 mm.s^{-1}, E_d = 288 J.cm^{-3}). This behaviour could be explained through the reversible character of the HA transformation. Liao et al. [37] studied the thermal decomposition and reconstitution of HA after heating at 1500ºC and cooling at a rate of 10ºC/min under air. They observed that the TTCP and α-TCP phases reconstructed gradually into HA, reaching a complete reconstitution under 1100ºC during the cooling phase. The different cooling rates and heat distributions produced by using different scanning speeds during the PBSLP process could affect differently to the decomposition and reconstitution behaviour of HA. However, to better understand this behaviour a deeper study on the effect of the cooling rate on the HA phase transition should be performed.

Additionally, it was observed that a higher E_d or lower scanning speed favoured the burnout and the corresponding removal of graphite (4.6 wt.% graphite at 288 J.cm^{-3}).

3.2.2 Second approach: HA complex parts

The printing of HA complex parts was performed in parallel to the previous approach. Not enough amount of ClA powder was available to produced solid parts at the time of the study. Therefore, only the feedstock powder HA_5G composed of HA and a 5 wt. % of graphite was used. The 3D model used and the resulting parts are shown in Figure 14. Both samples were printed at 240 J.cm^{-3} (30 W, 25 mm.s^{-1}) following the same hexagonal laser strategy. It is important to note that even if this combination of printing parameters did not show a good sintering/melting of the powder during the first approach, it was possible to print solid parts with a certain height. We could hypothesize that the changes in the thermal conductivity with the number of layers made possible the densification of the powder even if at the first layers the energy input was too low to sinter/melt the powder.
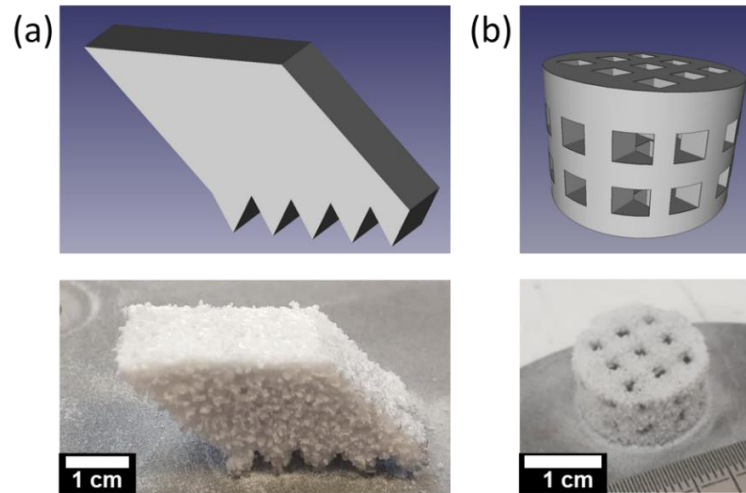

Figure 14. 3D model and printed HA complex parts: (a) HA_Trapezoid and (b) HA_Scaffold

Figure 15 shows the three-dimensional reconstructions of the printed samples using X-ray micro-computed tomography. Both parts presented a surface with high roughness. Two kinds of porosity were observed during the analysis of the internal microstructures. In Figure 15b it can be observed a homogeneous interconnected porosity presents on the whole volume of the samples together with a closed porosity of smaller size.

We found two possible hypotheses for the formation of the small closed porosity. A first option relates this kind of porosity (blowholes) to the pinholes previously observed in the surface of the samples of the first approach (Figure 9). The origin of these pores would be the formation of CO and CO_2 microbubbles during the graphite burnout in the liquid which remains enclosed in the microstructure. This kind of defect

is common in the processing of metals containing carbon [38,39]. Our second hypothesis is that this porosity is originated from the decomposition of the carbonate present in the structure of the HA used as raw material. AB-type carbonated apatite starts to decompose at about 400ºC releasing mainly CO_2. Since AB-type carbonated HA retains its apatite structure and partly the carbonates groups at 1100ºC, it has been useful for the production of porous carbonated apatite ceramics intended for bone tissue engineering scaffolds [40].

An analysis of the cross-section and the volume of the parts shows a distortion of the parts and the presence of cracks due to the high stresses to which the material was submitted during the printing process. The total porosity of these parts was found to be around 24% of the total volume. The designed toothed bottom surface of the sample HA_Trapezoid facilitated the detachment of the part from the substrate surface. However, the HA_scaffold sample suffered some deterioration due to the detachment using the homemade endless diamond wire saw.
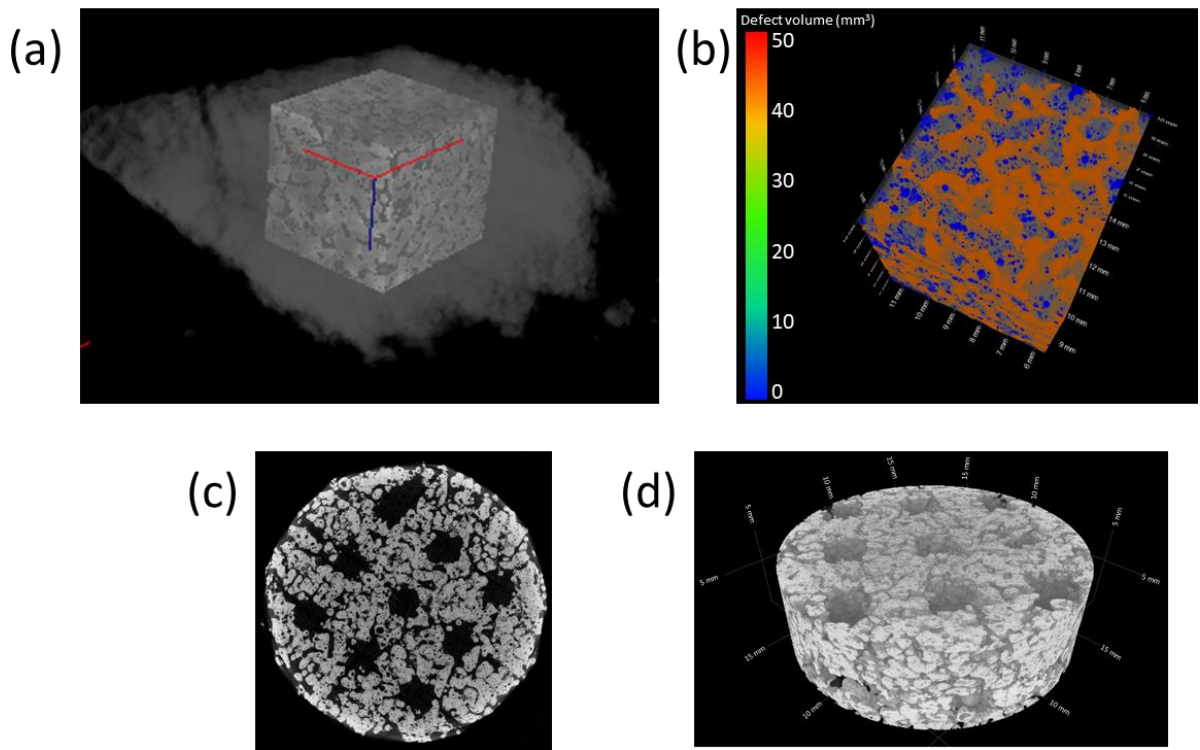

Figure 15. Visualization obtained using X-ray micro-computed tomography of the two kinds of printed parts: (a) Selection of the region of interest in HA_Trapezoid sample (b) Analysis of the porosity distribution in the region of interest (blue: closed porosity, orange: interconnected porosity) (c) Cross-section view of HA_Scaffold in the X-Y plane. (d) Volume analysis of the HA_Scaffold sample.

3.2.3 Third approach: HA cylinders

The previous approaches were carried out to evaluate the results of using different powder feedstock and printing parameters on the final composition and morphology of the printed parts. This approach instead, focused on the evaluation of the capacity of the HA_10G feedstock combined with an energy density of 96 J.cm^{-3} to produce solid parts with a certain shape intended for mechanical testing. A change of the laser strategy (from hexagonal to zig-zag) and parameters as needed to reduce the printing time of solid parts. The comparison between the time needed for the printing of the parts is done by calculating the build rate coefficient (B, cm^3.h^{-1}) (or productivity) of the process. This coefficient indicates the volume of material produced per hour and is proportional to the layer thickness, hatch distance, and laser scanning speed (equation 4). The higher the build rate the more productive will be the printing process [41].

$$B = v_{scan} \cdot h_{space} \cdot t_{layer} \tag{6}$$

Then, for the printing of the samples of the second approach, a $B = 0.45\ cm^3.h^{-1}$ was calculated while for this approach a $B = 1.35\ cm^3.h^{-1}$ was obtained. This productivity is three times higher than the previous one. Only the laser power and the scanning speed were modified (from 30 W, 25 mm.s^{-1} to 36W, 75 mm/s). Of course, this calculation should be taken as an approximation since factors like the overlapping rate of the layers are not taken into account. Moreover, this change of parameters does not aim to reach the maximum material processing speed of the PBSLP process but to speed up the process to facilitate the production of several cylinders intended for the analysis of the mechanical properties. The produced cylinders with 10 mm of diameter and 15 mm of height are shown in Figure 16. The change in colour (from greyish powder to brown) could be due to the presence of the secondary phases in the sample. It was not detected any important variation of the colour after the thermal treatment, which could indicate a not complete HA reconstruction. They were analysed chemically, structurally, and mechanically.
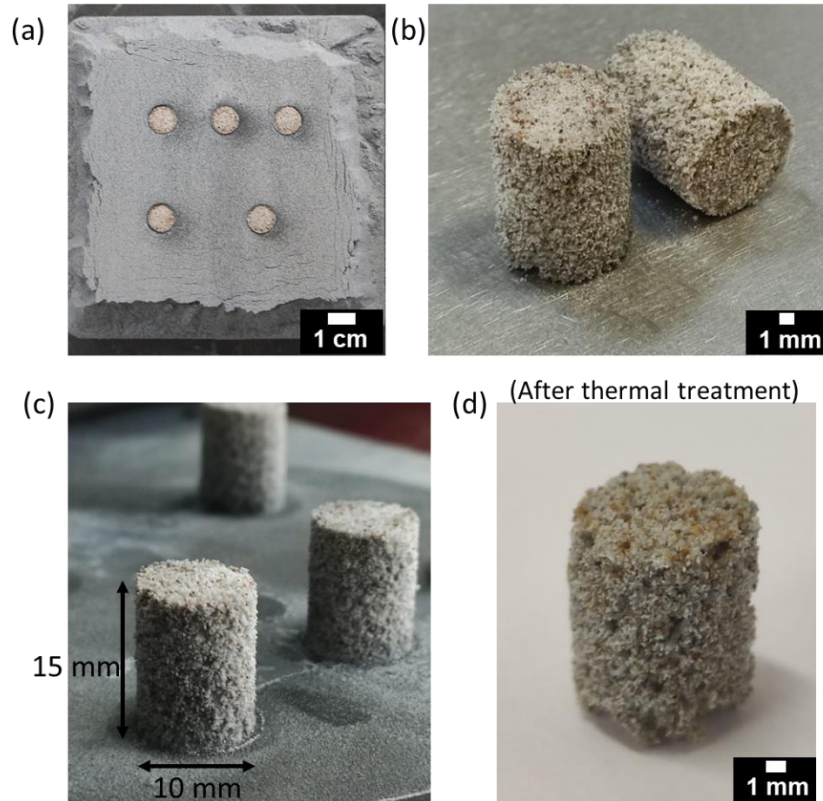
Figure 16. Photographs of HA cylinders samples produced by PBSLP at 96 J.cm^{-3} and a zig-zag laser scanning strategy (5 passes). (a) As printed, (b) after substrate removal, (c) general view, (d) sample after thermal-treatment.

The Figure 17a shows the Raman spectrum of the HA_Cyl sample in comparison with the TTCP, HA, and α-TCP spectra for comparison. The spectrum shows a contribution of the three calcium phosphate phases; however, the relative intensity of the bands is different from the one found for the samples produced during the first approach. The relative intensity related to the HA band is higher than the rest of the phases indicating a low phase transition. The X-ray diffractogram of the HA_Cyl sample before and after been post-treated is shown in Figure 17b. This result confirms the higher presence of the HA phase to the other phases in the HA_Cyl sample, these residual phases become invisible in the diffractogram after the thermal treatment. as was already observed in the Raman spectrum. Almost no presence of graphite was detected through XRD analysis. Once the sample is submitted to the thermal treatment, even a higher proportion of HA is detected, thus indicating a possible reverse phase transition from the others two phases (TTCP and α-TCP) into HA. Once again it can be observed that the crystal orientation of HA has been affected after PBSLP process (it is reflected in the change of the HA lines intensities).
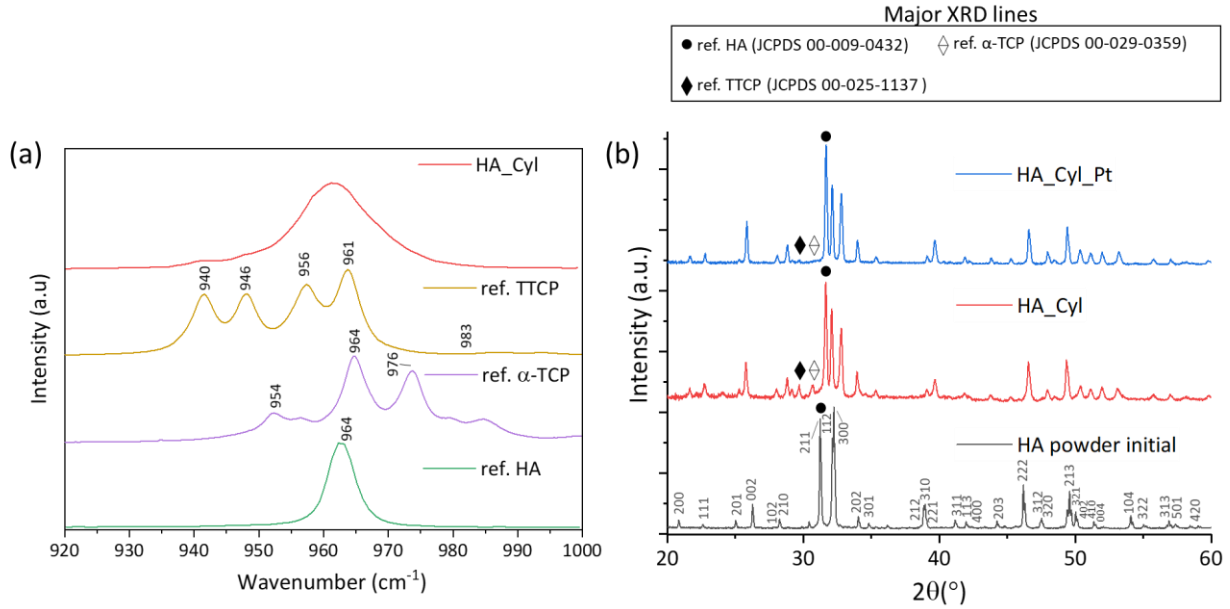
Figure 17. (a) Raman spectrum and (b) X-ray diffractograms were obtained for the cylinders printed at 96 J.cm^{-3}.

The FTIR spectra of the initial HA powder, the as-printed HA_Cyl, and after its post-treatment are shown in Figure 18. First, the presence of structural carbonate impurities located at the A and B sites (hydroxyl and phosphate sites, respectively) of apatite structure in the initial powder was detected [42]. It is observed from the bands at 1454 cm^{-1} and 877 cm^{-1} in the three samples. However, a decrease in their intensities is detected after each process step being almost invisible after the post-treatment of the cylindric sample. All the characteristic frequencies of PO4^{3-} modes [42] together with the bands corresponding to the structural OH^{-} of HA can also be found in the spectrum of the initial powder. Once the PBSLP process is performed to produce the HA_Cyl sample, the PO4^{3-} bands corresponding to TTCP and α-TCP appeared in the spectrum (through the broadening of the bands) confirming a partial phase transition. Bands corresponding to the structural OH^{-} become invisible due to the loss of intensity. It is after the post-treatment of the cylinder at high temperature that the bands corresponding to the HA phase recover a certain intensity becoming sharper, indicating that a reverse phase transition occurred.
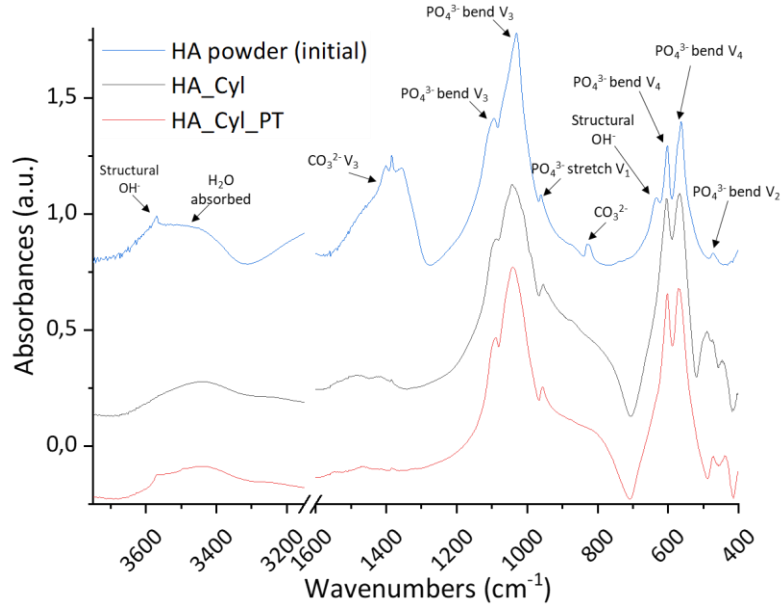
Figure 18. FTIR spectra of HA_Cyl and HA_Cyl_PT samples.

General information related to the microstructure and mechanical properties of HA_Cyl samples before and after the thermal treatment is offered in Table 6. Directional dimensions of the printed samples showed small variations to the dimensions of the original 3D model (10 x 15 mm). In laser processing of metals, the dimensional accuracy was found to be affected by two main factors, the solidification shrinkage and the mode of laser track filling and width [43]. Post-treatment of the sample did not show significant variations in the sample dimensions.

Table 6. Average directional dimensions (N=10, mean ± standard deviation), total porosity, relative densities (Archimedes and geometrical (N=10, mean ± standard deviation)), and preliminary result on compression strength (N=3, mean ± standard deviation) of HA cylinders before and after the post-treatment.

Sample	Directional dimensions		Total porosity (CT) (vol. %)	Relative density (Archimedes) (g.cm^{-3})	Relative density (Geometrical) (g.cm^{-3})	Compression strength (MPa)
	Height (mm)	Diameter (mm)				
HA_Cyl	14.6±0.4	11.2±0.1	50	2.77±0.02	2.47±0.10	0.010
HA_Cyl_PT	14.7±0.4	11.2±0.1	48	2.97±0.04	2.48±0.07	0.049±0.001

Figure 19 shows the three-dimensional reconstructions (region-of-interest) of the samples (before and after thermal treatment) using X-ray micro-computed tomography. The same kind of porosities (closed and interconnected) was observed for both samples, which was similar to the observed in the samples obtained during the second approach (HA_Trapezoid / HA_Scaffold) (Figure 15). Although a higher porosity was obtained for the last ones. The comparison between the two types of density values measured by two different methods (Archimedes and geometrical) gave us an idea of the porosity of the samples. Obtaining a higher value by Archimedes indicates that an internal open porosity exists. Its comparison with the initial HA powder density (3.16 g.cm^{-3}) also confirms the porosity observed by the CT technique (48 and 50 vol. % before and after thermal treatment, respectively) which is very close to the common cancellous bone porosity 50-90% [44]). Between the two different samples, the higher density obtained after post-treatment indicates that higher densification of the part occurred during the post-treatment which could improve their mechanical properties. This hypothesis is supported by the higher compression strength obtained for the sample after post-treatment (0.049±0.001 MPa) compared with the initial one (0.010 MPa). However, it is still lower than the strength reported for cancellous bone (1-12 MPa) [44].

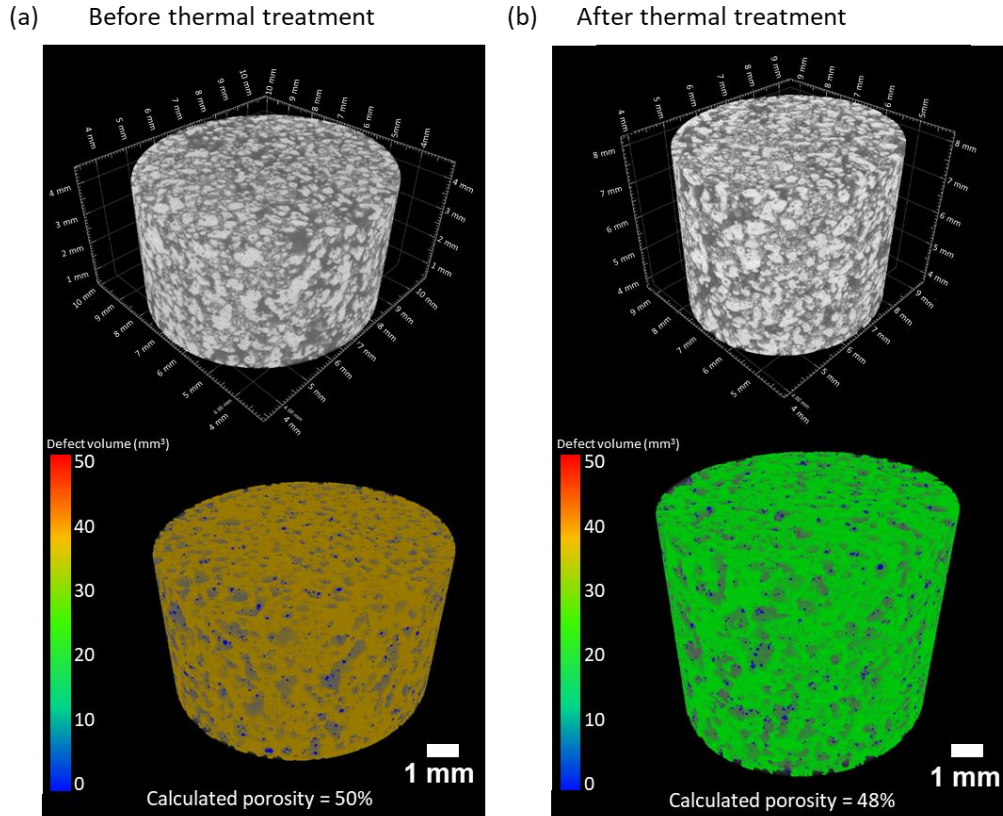(a)   Before thermal treatment   (b)   After thermal treatment

Figure 19. Visualization was obtained using X-ray micro-computed tomography of the sample HA_Cyl (a) before and (b) after the thermal treatment. Upper: Volume analysis of the samples. Down: Analysis of the porosity distribution in the region of interest (blue: closed porosity, orange and green: interconnected porosity

3.3 Heuristic procedure to determine the fixed PBSLP parameters

Heuristic research on the process parameters for the printing of CaP powders with graphite was carried out. A series of observations were obtained (underlined text) allowing us to reduce the range of parameters to evaluate during this work, thus fixing some of them. These first observations together with a review of the literature on laser processing of different materials explain the importance of these parameters and the reason for choosing determined values:

3.3.1   Atmosphere

During our study, the presence of oxygen in the chamber atmosphere was observed to have an important factor for the laser-induced ignition and combustion of graphite powder. This reaction can be described as exothermic (heat is evolved during the reaction), combustion (carbon burnt in presence of oxygen), and combination (carbon combines with oxygen to form carbon dioxide

and carbon monoxide) reaction. Graphite starts reacting (burning) with O_2 above 700-800ºC producing CO_2 and CO gases that will escape into the atmosphere leaving a porosity in the printed parts that will depend on the graphite volume fraction used [45]. The quantities of CO_2, CO and effective heat of reaction depend on the amount of oxygen and carbon available during the reaction [46]. The reactions taking place can be described as:

$$C_{(s)} + O_{2(g)} \rightarrow CO_{2(g)} \tag{7}$$

$$2C_{(s)} + O_{2(g)} \rightarrow 2CO_{(g)} \tag{8}$$

3.3.2 Powder compression

The compression of the powder bed was evaluated and an improvement on the surface finishing was observed when the powder was compacted before the laser scanning. It is known that the spreading and compression of the powder have an important effect on the properties of the printed parts. Beitz et al. [47] offered an interesting summary of the results obtained by different authors on the spreading and compression of powder beds with different devices. They concluded, through the study of the spreading of nylon PA12 powders, that an even compression of the powder bed is better achieved when using both, a scraper or blade and a counter-rotating roller. This combination, which is used in the present study, results in a more uniform and dense powder bed lowering the surface finish roughness of the parts. Sofia et al. [48] verified the effect of the compression of glass beads powder beds by bending tests indicating that the final sintered resistance increases by 198% in the case of compressed fine powder (x_{50} = 16 µm). However, it was pointed out that with the increase in the particle diameter, the compression process loses effectiveness. The effect of the roller-spreading parameters was studied by Zhang et al. [49] via discrete element simulation. They stated that lower roller translational velocity, higher roller diameter, and higher powder layer thickness increase the uniformity and density of the powder bed, although further research and experimental validation still have to be carried out to provide a more reliable basis for the optimization of the roller-spreading parameters.

3.3.3 Scanning strategy

During our preliminary tests, it was observed that the laser scan strategy had also a high influence on the quality of the parts. Precisely, the "track overlapping" or the repetition of different laser scans/passes over the same powder particles during the same layer step favoured the sintering/melting of the parts. This parameter has been rarely investigated, however, Changpeng et al. [50] offered a study on the prediction of the effect of the overlap rate and pattern on the residual stress (caused by the extremely uneven temperature distribution) induced

by the island scanning strategy during a selective laser process. Some of their findings were that an overlap rate of 25% - 50% for a general island size (between 1 x 1 mm^2 and 10 x 10 mm^2) and a laser vertical re-scanning (90º rotation between layers) together with a short scanning length were recommended to reduce the residual stress.

3.3.4 Laser defocusing

The influence of the laser defocusing by displacing the building platform in the z-axis was also evaluated. It was found that the defocusing strongly affects the laser-material interaction producing important variations in the final properties of the parts. It is known that the defocus distance alters the laser spot size and for hence the melt pool size. In addition, the direction in which the stage is moved in the z-axis is known to be a significant factor [12,51]. The production of solid parts was not possible when the laser was completely focused. A laser defocus of 3 cm downward the focus plane (positive sense) was tested and it allowed the densification of the parts. This laser defocus value distance was kept for the present study.

3.3.5 Substrate

The direct printing on the stainless-steel printing platform (absence of substrate), as well as the use of stainless steel and TA6V discs coated with HA, were evaluated in terms of printed part-building plane surface interaction. It was found that the distortion of the printed part was highly influenced by the kind of material used. The use of HA-coated discs seemed to improve this interaction enhancing the quality and density of the parts and their attachment to the substrate surface, better when using TA6V discs. In the field of laser processing (sintering/melting) of metallic powders, the influence of the material substrate has been widely studied. The substrates are commonly used to avoid the balling effect in powder melting and dislocation of the printed parts. The substrate surface roughness and wettability are known to have an effect on the spatter particle behaviour [52]. Shen et al. [53] studied the effect of the substrate on the temperature distribution during the laser processing of metallic powders. They confirmed the importance of the substrate material's thermal conductivity (k). When the thermal conductivity of the material used is poor the heat is confined in a small irradiated zone influencing negatively the quality of the parts. For the first printing layers, the heat absorbed by the powder bed is quickly transmitted to the substrate however when the process continues and the number of layers increases the distance between the irradiated powder layer and the substrate increases, reducing this heat transmission. Since the heat transference by the loose powder is much lower than by the full-density solid body of the substrate it leads to parts distortion (shrinkage and warping). For this

reason, it is common the utilization of the same material substrate as the powder being printed reducing the differences between thermal conductivities [54]. The thermal conductivities of the material employed have been reported in the literature [27,55,56]: stainless-steel (15 W.m^{-1}.K^{-1}), TA6V (7.1 W.m^{-1}.K^{-1}), HA (<3% porosity) coating (0.72-3 W.m^{-1}.K^{-1}) and HA powder (0.10-0.15 W.m^{-1}.K^{-1}). Through our observation, we could hypothesize that the lower differences between thermal conductivities of TA6V discs coated with HA and the HA powder bed, compared when using stainless steel, reduce the distortion and warping of the printed solid parts.

4. Conclusions

The present study shows our research on the PBSLP process of ceramic calcium phosphate powders. HA and ClA powders were mixed with graphite as an absorptance additive to be used as process feedstock. A preliminary analysis of the literature and heuristic research of the printing parameters was performed to close the wide range of parameters that the PBSLP technique involves fixing some of the parameters as the starting point. Three different approaches were employed for the analysis of materials feedstock performance.

First, the printing of laser-induced circular patterns at different printing parameters allowed us to obtain a process window for each one of the powders prepared and compare them. The absence of absorption additive made impossible the processability of the ceramic powder due to the low laser absorption. Then, it was observed that for blends containing 5 and 10 wt. % of graphite the higher the amount of additive the higher was the sintering/melting capacity of the blend. These circular samples were analysed microscopically, chemically, and structurally showing a phase transition for the powder composed of HA into TTCP and α-TCP. Phase proportion was dependent on the E_d used during the process and the amount of graphite. The HA powder feedstock containing a 10 wt. % of graphite, printed at an energy density of 288 J.cm^{-3} (laser power: 36 W; scanning speed: 25 mm.s^{-1}) showed the lowest effect of the balling phenomena and low phase transition after the process (46.5 wt.% HA). In this first approach, the sample ClA_5G showed the most outstanding results due to its inherent higher thermal stability without phase transition. All samples showed balling phenomena, however, the use of ClA_5G with a high E_d and HA_10G with low E_d (in the range studied) produced smoother surface finishing of the samples.

The second approach was performed in parallel to the first one. The printing of complex samples was achieved using the HA_5G feedstock and the same hexagon-based laser scan strategy as in the first approach. However, the combination of printing parameters used (laser power: 30 W, scanning speed: 25

mm.s^{-1}, E_d: 240 J.cm^{-3}) yielded a too slow build rate needing long times to print samples in series. The total porosity of these samples was 24%.

Through the third approach, HA_10G powder feedstock was used to achieve the production of solid cylindrical samples in a faster way. An energy density of 96 J.cm^{-3} (laser power: 36 W, scanning speed: 75 mm.s^{-1}) together with a strategy based on the overlapping of 5 laser passes for each printing laser were the parameters used. Morphology, chemical composition, and mechanical properties analyses of the cylinders before and after their treatment at high temperature were carried out. It was found that a phase transition of the initial HA powder into other phases occurred after their printing. This transition was partially reverted by the thermal treatment. This treatment also enhanced the compression strength of the sample from 0.010 MPa to 0.049±0.001 MPa. Indeed, it slightly increased the density of the part from 2.77±0.02 to 2.97±0.04. However, further research should be done on the improvement of the low mechanical properties observed through optimization of initial formulation, operating conditions, and/or additional post-treatments.

In conclusion, the processability of calcium phosphate powders in a PBSLP was possible by addition of graphite as absorption additive. Phase transition of HA into other phases was evaluated with different powder feedstock and printing parameters. Solid samples were successfully printed with a majority of HA phases in their composition. ClA showed promising results as starting powder feedstock to HA mainly due to its higher thermal stability, avoiding any phase change. This is the first step for the direct production of calcium phosphate bone substitutes through the PBSLP process. A deeper investigation should be made on the use of ClA powder as feedstock for the printing of solid parts. Further studies on the improvement of the mechanical properties of the parts could open a new possibility for the production of bioceramic scaffolds with interconnected porosity with potentially enhanced bioactive properties.

5. Acknowledgments

6. Author contributions

P. Navarrete-Segado, C. Frances, M. Tourbin, and D. Grossin designed the followed methodology. P. Navarrete-Segado drafted the manuscript and conducted the majority of experiments. C. Tenailleau and B. Duployer performed the CT experiments. D. Grossin also supervised the project.

7. Data availability

The raw/processed data required to reproduce these findings cannot be shared at this time as the data also forms part of an ongoing study.

8. REFERENCES

[1] D. Grossin, A. Montón, P. Navarrete-Segado, E. Özmen, G. Urruth, F. Maury, D. Maury, C. Frances, M. Tourbin, P. Lenormand, G. Bertrand, A review of additive manufacturing of ceramics by powder bed selective laser processing (sintering / melting): Calcium phosphate, silicon carbide, zirconia, alumina, and their composites, Open Ceramics. 5 (2021) 100073. https://doi.org/10.1016/j.oceram.2021.100073.

[2] S. Eosoly, D. Brabazon, S. Lohfeld, L. Looney, Selective laser sintering of hydroxyapatite/poly-ε-caprolactone scaffolds, Acta Biomaterialia. 6 (2010) 2511–2517. https://doi.org/10.1016/j.actbio.2009.07.018.

[3] L. Hao, M.M. Savalani, Y. Zhang, K.E. Tanner, R.J. Heath, R.A. Harris, Characterization of selective laser-sintered hydroxyapatite-based biocomposite structures for bone replacement, Proceedings of the Royal Society A: Mathematical, Physical and Engineering Sciences. 463 (2007) 1857–1869. https://doi.org/10.1098/rspa.2007.1854.

[4] Y. Xia, P. Zhou, X. Cheng, Y. Xie, C. Liang, C. Li, S. Xu, Selective laser sintering fabrication of nano-hydroxyapatite/poly-ε-caprolactone scaffolds for bone tissue engineering applications, Int J Nanomedicine. 8 (2013) 4197–4213. https://doi.org/10.2147/IJN.S50685.

[5] F. Cruz, Fabrication of HA/PLLA Composite Scaffolds for Bone Tissue Engineering Using Additive Manufacturing Technologies, in: M. Elnashar (Ed.), Biopolymers, Sciyo, 2010. https://doi.org/10.5772/10264.

[6] R. Donate, M. Monzón, M.E. Alemán-Domínguez, Additive manufacturing of PLA-based scaffolds intended for bone regeneration and strategies to improve their biological properties, E-Polymers. 20 (2020) 571–599. https://doi.org/10.1515/epoly-2020-0046.

[7] H. Zeng, J.L. Pathak, Y. Shi, J. Ran, L. Liang, Q. Yan, T. Wu, Q. Fan, M. Li, Y. Bai, Indirect selective laser sintering-printed microporous biphasic calcium phosphate scaffold promotes endogenous bone regeneration via activation of ERK1/2 signaling, Biofabrication. 12 (2020) 025032. https://doi.org/10.1088/1758-5090/ab78ed.

[8] C. Shuai, P. Li, J. Liu, S. Peng, Optimization of TCP/HAP ratio for better properties of calcium phosphate scaffold via selective laser sintering, Materials Characterization. 77 (2013) 23–31. https://doi.org/10.1016/j.matchar.2012.12.009.

[9] L. Ferrage, G. Bertrand, P. Lenormand, Dense yttria-stabilized zirconia obtained by direct selective laser sintering, Additive Manufacturing. 21 (2018) 472–478. https://doi.org/10.1016/j.addma.2018.02.005.

[10] C. Colin, J.-D. Bartout, E. Shaker, Osseomatrix patent - WO2014154901A1, WO2014154901A1, 2014.

[11] K.G. Prashanth, S. Scudino, T. Maity, J. Das, J. Eckert, Is the energy density a reliable parameter for materials synthesis by selective laser melting?, Materials Research Letters. 5 (2017) 386–390. https://doi.org/10.1080/21663831.2017.1299808.

[12] P. Leo, M. Cabibbo, A. Del Prete, S. Giganto, S. Martínez-Pellitero, J. Barreiro, Laser Defocusing Effect on the Microstructure and Defects of 17-4PH Parts Additively Manufactured by SLM at a Low Energy Input, Metals. 11 (2021) 588. https://doi.org/10.3390/met11040588.

[13] I. Demnati, D. Grossin, O. Marsan, G. Bertrand, G. Collonges, C. Combes, M. Parco, I. Braceras, J. Alexis, Y. Balcaen, C. Rey, Comparison of Physical-chemical and Mechanical Properties of

Chlorapatite and Hydroxyapatite Plasma Sprayed Coatings, The Open Biomedical Engineering Journal. 9 (2015). https://doi.org/10.2174/1874120701509010042.

[14] K. Tõnsuaadu, K.A. Gross, L. Plūduma, M. Veiderma, A review on the thermal stability of calcium apatites, J Therm Anal Calorim. 110 (2012) 647–659. https://doi.org/10.1007/s10973-011-1877-y.

[15] K. Yanagisawa, J.C. Rendon-Angeles, N. Ishizawa, S. Oishi, Topotaxial replacement of chlorapatite by hydroxyapatite during hydrothermal ion exchange, American Mineralogist. 84 (1999) 1861–1869. https://doi.org/10.2138/am-1999-11-1213.

[16] M. Tourbin, F. Brouillet, B. Galey, N. Rouquet, P. Gras, N. Abi Chebel, D. Grossin, C. Frances, Agglomeration of stoichiometric hydroxyapatite: Impact on particle size distribution and purity in the precipitation and maturation steps, Powder Technology. 360 (2020) 977–988. https://doi.org/10.1016/j.powtec.2019.10.050.

[17] P. Navarrete-Segado, C. Frances, D. Grossin, M. Tourbin, Tailoring hydroxyapatite microspheres by spray-drying for powder bed fusion feedstock., Adv. Powder Technol. (Submitted). (2021).

[18] I. Demnati, D. Grossin, C. Combes, M. Parco, I. Braceras, C. Rey, A comparative physico-chemical study of chlorapatite and hydroxyapatite: from powders to plasma sprayed thin coatings, Biomed. Mater. 7 (2012) 054101. https://doi.org/10.1088/1748-6041/7/5/054101.

[19] L. Lutterotti, S. Matthies, H. Wenk, MAUD: a friendly Java program for material analysis using diffraction, UCr: Newsletter of the CPD. 21 (1999) 14–15.

[20] C.A. Schneider, W.S. Rasband, K.W. Eliceiri, NIH Image to ImageJ: 25 years of image analysis, Nat Methods. 9 (2012) 671–675. https://doi.org/10.1038/nmeth.2089.

[21] Implants for surgery ISO 13175-3 2012 — Calcium phosphates — Part 3: Hydroxyapatite and beta-tricalcium phosphate bone substitutes, (2008).

[22] N.K. Tolochko, Y.V. Khlopkov, S.E. Mozzharov, M.B. Ignatiev, T. Laoui, V.I. Titov, Absorptance of powder materials suitable for laser sintering, Rapid Prototyping Journal. 6 (2000) 155–161. https://doi.org/10.1108/13552540010337029.

[23] T. Laumer, T. Stichel, M. Sachs, P. Amend, M. Schmidt, Qualification and modification of new polymer powders for laser beam melting using Ulbricht spheres, in: P. da Silva Bártolo, A. de Lemos, A. Pereira, A. Mateus, C. Ramos, C. Santos, D. Oliveira, E. Pinto, F. Craveiro, H. da Rocha Terreiro Galha Bártolo, H. de Amorim Almeia, I. Sousa, J. Matias, L. Durão, M. Gaspar, N. Fernandes Alves, P. Carreira, T. Ferreira, T. Marques (Eds.), High Value Manufacturing: Advanced Research in Virtual and Rapid Prototyping, CRC Press, 2013: pp. 255–260. https://doi.org/10.1201/b15961-48.

[24] H.C.H. Ho, W.L. Cheung, I. Gibson, Effects of graphite powder on the laser sintering behaviour of polycarbonate, Rapid Prototyping Journal. 8 (2002) 233–242. https://doi.org/10.1108/13552540210441148.

[25] T.J. Levingstone, M. Ardhaoui, K. Benyounis, L. Looney, J.T. Stokes, Plasma sprayed hydroxyapatite coatings: Understanding process relationships using design of experiment analysis, Surface and Coatings Technology. 283 (2015) 29–36. https://doi.org/10.1016/j.surfcoat.2015.10.044.

[26] V.V. Sobolev, J.M. Guilemany, Flattening of Droplets and Formation of Splats in Thermal Spraying: A Review of Recent Work— Part, Journal of Thermal Spray Technology. 8 (1999) 301–314.

[27] M. Chambard, Revêtements nanostructurés d'hydroxyapatite multisubstituée élaborés par projection de suspension par plasma inductif : de la chimie du précurseur aux propriétés mécaniques et biologiques, (2019) 331.

[28] J. Liu, B. Zhang, C. Yan, Y. Shi, The effect of processing parameters on characteristics of selective laser sintering dental glass-ceramic powder, Rapid Prototyping Journal. 16 (2010) 138–145. https://doi.org/10.1108/13552541011025861.

[29] M. Prakasam, J. Locs, K. Salma-Ancane, D. Loca, A. Largeteau, L. Berzina-Cimdina, Fabrication, Properties and Applications of Dense Hydroxyapatite: A Review, J Funct Biomater. 6 (2015) 1099–1140. https://doi.org/10.3390/jfb6041099.

[30] L. Moniz, Q. Chen, G. Guillemot, M. Bellet, C.-A. Gandin, C. Colin, J.-D. Bartout, M.-H. Berger, Additive manufacturing of an oxide ceramic by laser beam melting—Comparison between finite

element simulation and experimental results, Journal of Materials Processing Technology. 270 (2019) 106–117. https://doi.org/10.1016/j.jmatprotec.2019.02.004.

[31] S. Liu, H. Guo, Balling Behavior of Selective Laser Melting (SLM) Magnesium Alloy, Materials (Basel). 13 (2020) 3632. https://doi.org/10.3390/ma13163632.

[32] D. Gu, Y. Shen, Balling phenomena in direct laser sintering of stainless steel powder: Metallurgical mechanisms and control methods, (2009). https://doi.org/10.1016/J.MATDES.2009.01.013.

[33] Z. Wang, X. Wang, X. Zhou, G. Ye, X. Cheng, P. Zhang, Investigation into Spatter Particles and Their Effect on the Formation Quality During Selective Laser Melting Processes, Computer Modeling in Engineering & Sciences. 124 (2020) 243–263. https://doi.org/10.32604/cmes.2020.09934.

[34] M.H. Leipold, T.H. Nielsen, E.C. de Wys, The Effect of Grain Boundaries on Mechanical Behavior in Polycrystalline Ceramics, Technical Report. (1967) 16.

[35] L. de A. Cavalcante, L.S. Ribeiro, M.L. Takeno, P.T.P. Aum, Y.K.P.G. Aum, J.C.S. Andrade, Chlorapatite Derived from Fish Scales, Materials. 13 (2020) 1129. https://doi.org/10.3390/ma13051129.

[36] E. García-Tuñón, R. Couceiro, J. Franco, E. Saiz, F. Guitián, Synthesis and characterisation of large chlorapatite single-crystals with controlled morphology and surface roughness, J Mater Sci Mater Med. 23 (2012) 2471–2482. https://doi.org/10.1007/s10856-012-4717-0.

[37] C.-J. Liao, F.-H. Lin, K.-S. Chen, J.-S. Sun, Thermal decomposition and reconstitution of hydroxyapatite in air atmosphere, Biomaterials. 20 (1999) 1807–1813. https://doi.org/10.1016/S0142-9612(99)00076-9.

[38] M. Hashiura, K. Mori, Formation of CO Macroblowholes during Solidification of Iron-Carbon Alloys Containing below 0.03% Carbon, (1988). https://doi.org/10.2355/TETSUTOHAGANE1955.74.6_1006.

[39] A. Goel, Material Science and Metallurgy: Fundamentals and Importance, Technical Publications, 2021.

[40] S.M. Barinov, J.V. Rau, S.N. Cesaro, J. Ďurišin, I.V. Fadeeva, D. Ferro, L. Medvecky, G. Trionfetti, Carbonate release from carbonated hydroxyapatite in the wide temperature rage, J Mater Sci: Mater Med. 17 (2006) 597–604. https://doi.org/10.1007/s10856-006-9221-y.

[41] N. Makoana, I. Yadroitsava, H. Möller, I. Yadroitsev, Characterization of 17-4PH Single Tracks Produced at Different Parametric Conditions towards Increased Productivity of LPBF Systems—The Effect of Laser Power and Spot Size Upscaling, Metals. 8 (2018) 475. https://doi.org/10.3390/met8070475.

[42] C. Rey, O. Marsan, C. Combes, C. Drouet, D. Grossin, S. Sarda, Characterization of Calcium Phosphates Using Vibrational Spectroscopies, in: B. Ben-Nissan (Ed.), Advances in Calcium Phosphate Biomaterials, Springer Berlin Heidelberg, Berlin, Heidelberg, 2014: pp. 229–266. https://doi.org/10.1007/978-3-642-53980-0_8.

[43] L. Zhang, S. Zhang, H. Zhu, Z. Hu, G. Wang, X. Zeng, Horizontal dimensional accuracy prediction of selective laser melting, Materials & Design. 160 (2018) 9–20. https://doi.org/10.1016/j.matdes.2018.08.059.

[44] T.-R. Kim, M.-S. Kim, T.S. Goh, J.S. Lee, Y.H. Kim, S.-Y. Yoon, C.-S. Lee, Evaluation of Structural and Mechanical Properties of Porous Artificial Bone Scaffolds Fabricated via Advanced TBA-Based Freeze-Gel Casting Technique, Applied Sciences. 9 (2019) 1965. https://doi.org/10.3390/app9091965.

[45] D.M. Crumpton, R.A. Laitinen, J. Smieja, D.A. Cleary, Thermal Analysis of Carbon Allotropes: An Experiment for Advanced Undergraduates, ACS Publications. (1996). https://doi.org/10.1021/ed073p590.

[46] Y. Wang, M. Zhang, S. Chang, S. Li, X. Huang, Laser-Induced Ignition and Combustion Behavior of Individual Graphite Microparticles in a Micro-Combustor, Processes. 8 (2020) 1493. https://doi.org/10.3390/pr8111493.

[47] S. Beitz, R. Uerlich, T. Bokelmann, A. Diener, T. Vietor, A. Kwade, Influence of Powder Deposition on Powder Bed and Specimen Properties, Materials. (2019). https://doi.org/10.3390/ma12020297.

[48] D. Sofia, M. Lupo, D. Barletta, M. Poletto, Validation of an Experimental Procedure to Quantify The Effects of Powder Spreadability on Selective Laser Sintering Process, Chemical Engineering Transactions. 74 (2019) 397. https://doi.org/10.3303/CET1974067.

[49] J. Zhang, Y. Tan, T. Bao, Y. Xu, X. Xiao, S. Jiang, Discrete Element Simulation of the Effect of Roller-Spreading Parameters on Powder-Bed Density in Additive Manufacturing, Materials. 13 (2020) 2285. https://doi.org/10.3390/ma13102285.

[50] C. Changpeng, J. Yin, H. Zhu, Z. Xiao, L. Zhang, X. Zeng, Effect of overlap rate and pattern on residual stress in selective laser melting, International Journal of Machine Tools and Manufacture. 145 (2019) 103433. https://doi.org/10.1016/j.ijmachtools.2019.103433.

[51] J. Metelkova, Y. Kinds, K. Kempen, C. de Formanoir, A. Witvrouw, B. Van Hooreweder, On the influence of laser defocusing in Selective Laser Melting of 316L, Additive Manufacturing. 23 (2018) 161–169. https://doi.org/10.1016/j.addma.2018.08.006.

[52] T. Furumoto, K. Egashira, K. Oishi, S. Abe, M. Yamaguchi, Y. Hashimoto, T. Koyano, A. Hosokawa, Experimental investigation into the spatter particle behavior of maraging steel during selective laser melting, JAMDSM. 15 (2021) JAMDSM0039–JAMDSM0039. https://doi.org/10.1299/jamdsm.2021jamdsm0039.

[53] X. Shen, Y. Wang, J. Yang, Effect of substrate on temperature field in selective laser sintering of metal powders, in: International Congress on Applications of Lasers & Electro-Optics, Laser Institute of America, Orlando, Florida, USA, 2009: pp. 821–829. https://doi.org/10.2351/1.5061650.

[54] S. Liu, S. Chang, H. Zhu, J. Yin, T. Wang, X. Zeng, Effect of substrate material on the molten pool characteristics in selective laser melting of thin wall parts, Int J Adv Manuf Technol. 105 (2019) 3221–3231. https://doi.org/10.1007/s00170-019-04540-1.

[55] S.S. Sib, J.W. Barlow, Measurement and prediction of the thermal conductivity of powders at high htemperatrues, (1994) 9.

[56] Thermal Conductivity of Metals, Metallic Elements and Alloys, (2005). https://www.engineeringtoolbox.com/thermal-conductivity-metals-d_858.html.
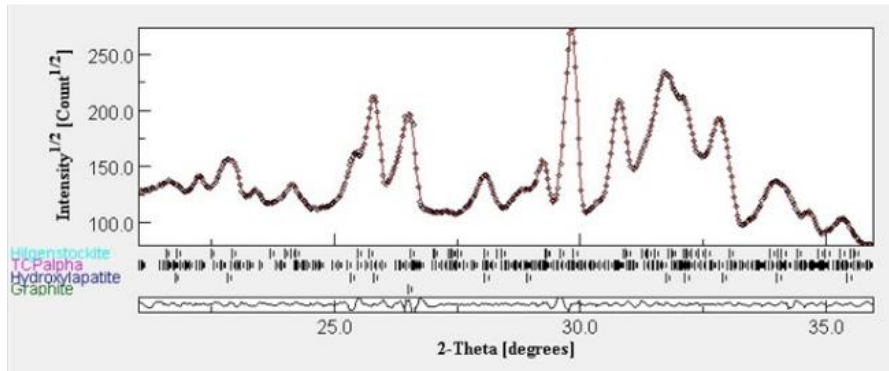
Supplementary information

Figure S1. Example of one plot of the Rietveld refinement of the HA laser-induced sample (HA_10G_96), with the Bragg reflections of each phase, labelled on the left. Hilgenstockite = TTCP phase.